

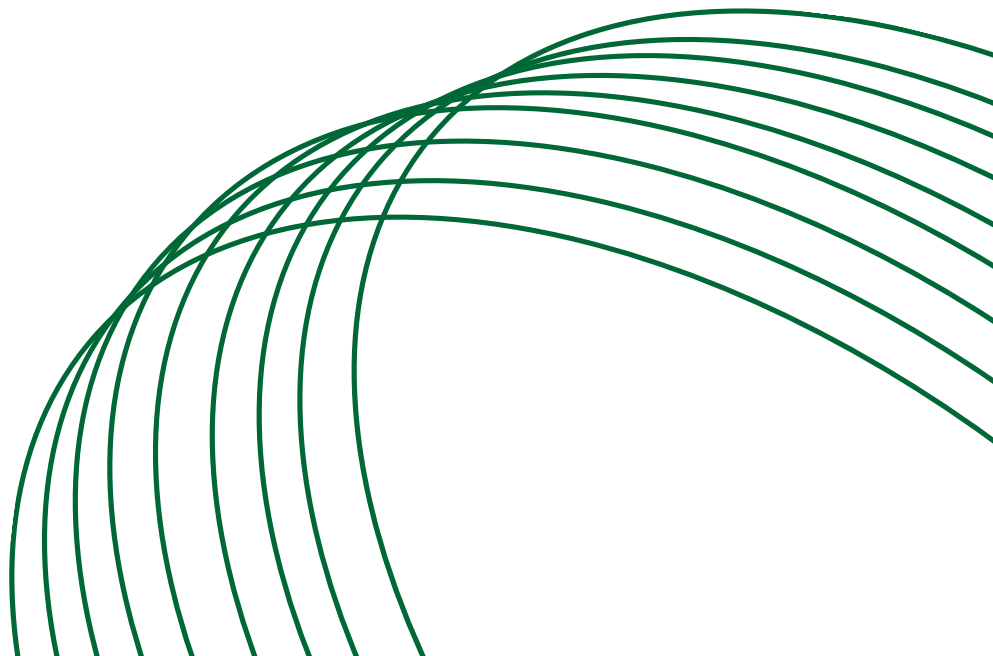
# **Rotary Inverted Pendulum**

Corso Federico  
Leto Andrea  
Tagliaferro Alberto  
Vazzoler Simone



**POLITECNICO**  
**MILANO 1863**

SCUOLA DI INGEGNERIA INDUSTRIALE  
E DELL'INFORMAZIONE





## Abstract

The selected project is the "Rotatory Inverted Pendulum," which consists of a rotary arm, a pendulum rod, a servo motor, and two encoders. These encoders measure the angles  $\theta$  (related to the rotary arm) and  $\alpha$  (related to the pendulum rod), representing the system's two degrees of freedom. The objective of this laboratory is to stabilize the system around its unstable equilibrium point.

To begin, we identified the system's physical parameters. Next, we designed a frequency-based controller that operates on the horizontal arm. Subsequently, we employed Pole Placement and LQG (Linear Quadratic Gaussian) regulators to address the stabilization problem. Finally, we developed a swing-up control law utilizing Partial Feedback Linearization and an Energy Controller.



Figure 1: Rotatory Inverted Pendulum.

# Contents

<b>1 Equations of Motion</b>	<b>1</b>
1.1 Analysis of the Kinematic Chain . . . . .	2
1.1.1 Position Analysis . . . . .	2
1.2 Lagrangian and Equations of Motion . . . . .	2
1.2.1 Kinetic and Potential Energy of the System . . . . .	2
1.2.2 Generalized and Dissipative Forces . . . . .	2
1.2.3 Non Linear Equations . . . . .	3
1.3 Linearization of the Equation of Motion . . . . .	3
1.3.1 Unstable Equilibrium . . . . .	3
1.3.2 Stable Equilibrium . . . . .	4
1.4 Simulation and Experiments . . . . .	5
1.4.1 Description of Experiment and Results . . . . .	5
1.4.2 Operative Notes . . . . .	5
<b>2 System Identification</b>	<b>6</b>
2.1 Identification of the Non Linear Model of the Rotary Inverted Pendulum . . . . .	6
2.1.1 Training Set . . . . .	7
2.1.2 Validation Set . . . . .	9
2.1.3 Frequency Domain Validation and Chirp Signal . . . . .	10
2.1.4 Residual Analysis . . . . .	12
<b>3 Frequency Based Control</b>	<b>13</b>
3.1 Open Loop Analysis . . . . .	13
3.2 Controller Design . . . . .	14
3.2.1 L(s) Design . . . . .	14
3.2.2 Stability . . . . .	15
3.2.3 Performances: Sensitivity Functions . . . . .	15
3.2.4 Behaviour of Alpha $G_{Y\alpha}(s)$ in the Closed-Loop System . . . . .	16
3.3 Performances: Step Response . . . . .	16
3.4 Experiment . . . . .	17
3.4.1 Experimental Behaviour of $G_{Y\alpha}(s)$ : Resonance . . . . .	18
<b>4 State Space Based Control</b>	<b>19</b>
4.1 Pole Placement Controller . . . . .	19
4.2 Luenberger Observer . . . . .	20
4.3 Linear Quadratic Gaussian Regulator . . . . .	21
4.3.1 LQ Infinity Control . . . . .	22
4.3.2 Kalman Filter . . . . .	23
4.4 Tracking of $\theta$ . . . . .	25
4.4.1 Pole Placement . . . . .	25
4.4.2 LQG Control . . . . .	26
4.4.3 Robustness of Tracking . . . . .	27
4.5 Experiments . . . . .	28
4.5.1 Pole Placement Experiments . . . . .	28
4.5.2 LQG Experiments . . . . .	30
4.5.3 Comparison and Final Notes . . . . .	32

<b>5 Swing Up Control</b>	<b>33</b>
5.1 Partial Feedback Linearization: P.F.L. . . . .	33
5.2 Energy Control . . . . .	33
5.2.1 Stabilizing Controller and Switching Logic . . . . .	34
5.2.2 The Extended Kalman Filter . . . . .	34
5.3 Validation of the Control Law . . . . .	34
5.3.1 Dealing with Initial Conditions . . . . .	34
5.3.2 Simulation and Experimental Results . . . . .	35
5.3.3 Repeatability . . . . .	36
<b>List of Figures</b>	<b>39</b>
<b>List of Tables</b>	<b>40</b>
<b>Bibliography</b>	<b>41</b>
<b>Appendix</b>	<b>43</b>

# 1. Equations of Motion

The equations of motion are derived through the Lagrangian approach. This requires only to compute the following quantities:

- The total Kinetic Energy of the system  $T_{tot}$  given by the sum of the kinetic energy of each body:

$$T_{tot} = \frac{1}{2} \sum_{i=1}^N (m_i \mathbf{v}_i^2 + J_i \omega_i^2) \quad (1.1)$$

- The total potential energy of the system  $V$
- The total viscous energy dissipation
- The generalized forces

To this aim, we start from the free body diagram of the system where we identify some useful parameters and points described in Table 5.8, that can be found in the appendix, and Figure 1.1.

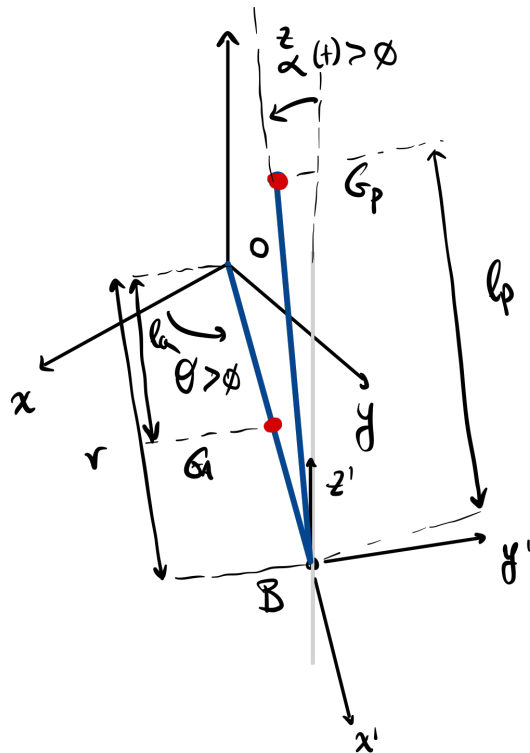


Figure 1.1: Free Body Diagram.

## 1.1 Analysis of the Kinematic Chain

The mechanism has two degrees of freedom, the angle  $\theta(t)$  described by the horizontal arm  $OB$  and the pendulum angle  $\alpha(t)$  measured with respect to the vertical direction.

### 1.1.1 Position Analysis

First we identify the position in the inertial frame of some notable points, such as the center of mass of both horizontal arm  $G_A$  and pendulum  $G_P$ , and the non actuated joint  $B$ .

$$G_A = \begin{pmatrix} x_{G_A}(t) = l_a \cos(\theta(t)) \\ y_{G_A}(t) = l_a \sin(\theta(t)) \\ z_{G_A}(t) = 0 \end{pmatrix}; \quad B = \begin{pmatrix} x_B(t) = r \cos(\theta(t)) \\ y_B(t) = r \sin(\theta(t)) \\ z_B(t) = 0 \end{pmatrix} \quad (1.2)$$

$$G_p = \begin{pmatrix} x_{G_p}(t) = r \cos(\theta(t)) + l_p \sin(\alpha(t)) \sin(\theta(t)) \\ y_{G_p}(t) = r \sin(\theta(t)) - l_p \sin(\alpha(t)) \cos(\theta(t)) \\ z_{G_p}(t) = l_p \cos(\alpha(t)) \end{pmatrix} \quad (1.3)$$

$G_p$  has been expressed in the inertial frame using the following transformation:  $G_p = B + R G'_p$ . Where the matrix  $R$  is the rotational transformation between the inertial frame and the non inertial frame centered at point  $B$  and  $G'_p$  has been expressed with respect to  $B$  as follows:

$$R = \begin{pmatrix} \cos(\theta(t)) & -\sin(\theta(t)) & 0 \\ \sin(\theta(t)) & \cos(\theta(t)) & 0 \\ 0 & 0 & 1 \end{pmatrix}; \quad G'_p = \begin{pmatrix} x_{G'_p}(t) = 0 \\ y_{G'_p}(t) = -l_p \sin(\alpha(t)) \\ z_{G'_p}(t) = l_p \cos(\alpha(t)) \end{pmatrix} \quad (1.4)$$

## 1.2 Lagrangian and Equations of Motion

First of all, we have to compute the Lagrangian ( $L$ ) which is given by the difference between kinetic and potential energy.

$$L = T_{tot} - V \quad (1.5)$$

### 1.2.1 Kinetic and Potential Energy of the System

The total kinetic energy  $T_{tot}$  can be expressed as:  $T_{tot} = T_{arm} + T_{pendulum}$ ; where the horizontal arm and pendulum terms can be computed, with the Konig theorem, as:

$$T_{arm} = \frac{1}{2} J_a \dot{\theta}^2; \quad T_{pendulum} = \frac{1}{2} m_p \mathbf{v}_p^2 + \frac{1}{2} J_p \dot{\alpha}^2 \quad (1.6)$$

with,

$$\mathbf{v}_p^2 = \dot{x}_p^2 + \dot{y}_p^2 + \dot{z}_p^2 \quad (1.7)$$

The potential energy  $V$  depends only from the gravitational force acting on the pendulum:

$$V = g l_p m_p (\cos(\alpha(t)) - 1) \quad (1.8)$$

Finally the Lagrangian will result as:

$$L = \frac{1}{2} m_p \mathbf{v}_p^2 + \frac{1}{2} J_p \dot{\alpha}^2 + \frac{1}{2} J_a \dot{\theta}^2 - g l_p m_p (\cos(\alpha(t)) - 1) \quad (1.9)$$

### 1.2.2 Generalized and Dissipative Forces

Consider now the two generalized coordinate  $\theta$  and  $\alpha$  as a vertical vector:

$$q(t)^T = [\theta(t) \ \alpha(t)] \quad (1.10)$$

and the generalized forces acting on them:

$$Q_1 = \tau - B_r \dot{\theta}; \quad Q_2 = -B_p \dot{\alpha} \quad (1.11)$$

### 1.2.3 Non Linear Equations

The Lagrange equation is given by:

$$\frac{\partial^2 L}{\partial t \partial \dot{q}_i} - \frac{\partial L}{\partial q_i} = Q_i \quad (1.12)$$

Finally the non linear equations of motion are obtained:

$$\begin{aligned} & \left( -m_p l_p^2 \cos(\alpha_t)^2 + m_p l_p^2 + m_p r^2 + J_a \right) \ddot{\theta} + (l_p^2 m_p \sin(2\alpha_t)) \dot{\theta} \dot{\alpha} \\ & + (-l_p m_p r \cos(\alpha_t)) \ddot{\alpha} + (l_p m_p r \sin(\alpha_t)) \dot{\alpha}^2 = \tau - B_r \dot{\theta} \end{aligned} \quad (1.13)$$

$$\begin{aligned} & (-2 l_p m_p r \cos(\alpha_t)) \ddot{\theta} + (-l_p^2 m_p \sin(2\alpha_t)) \dot{\theta}^2 + (2 m_p l_p^2 + 2 J_p) \ddot{\alpha} \\ & - 2 g l_p m_p \sin(\alpha_t) = -2 B_p \dot{\alpha} \end{aligned} \quad (1.14)$$

The torque applied at the base of the rotary arm is generated by the servo motor as described by:

$$\tau = \frac{\eta_g K_g \eta_m k_t (V_m - K_g k_m \dot{\theta})}{R_m} \quad (1.15)$$

This equation has been derived by applying Kirchhoff's Voltage Law and making the assumption that the motor inductance  $L_m$  is significantly smaller than its resistance, allowing us to neglect it. Thus, we can determine the motor current as follows:

$$I_m(t) = \frac{V_m(t) - k_m \omega_m(t)}{R_m(t)} \quad (1.16)$$

The motor torque is proportional to the voltage applied and is described as:

$$\tau_m(t) = \eta_m k_t I_m(t) \quad (1.17)$$

The Eq. 1.15 is finally computed considering the relationship between the motor torque and the real torque applied to the load (due to the gearbox transmission) is:

$$\tau(t) = \eta_g K_g \tau_m(t) \quad (1.18)$$

## 1.3 Linearization of the Equation of Motion

### 1.3.1 Unstable Equilibrium

Let  $z$  be the defined as follows (time dependency is neglected for simplicity):

$$z = [\theta; \alpha; \dot{\theta}; \dot{\alpha}; \ddot{\theta}; \ddot{\alpha}] \quad (1.19)$$

The non linear equations of motion (Eq. 1.13 and Eq. 1.14) are linearized around the unstable equilibrium position:

$$z_0 = [0; 0; 0; 0; 0; 0] \quad (1.20)$$

By evaluating the Jacobian at  $z_0$ , we obtain the following matrix:

$$\mathbb{J}_0 = \begin{bmatrix} 0 & 0 & B_r & 0 & m_p r^2 + J_a & -l_p m_p r \\ 0 & -2 g l_p m_p & 0 & 2 B_p & -2 l_p m_p r & 2 m_p l_p^2 + 2 J_p \end{bmatrix} \quad (1.21)$$

The corresponding linearized equations of motion are:

$$\begin{aligned} B_r \dot{\theta} + \ddot{\theta} (m_p r^2 + J_a) - \ddot{\alpha} l_p m_p r &= \tau \\ B_p \dot{\alpha} + \ddot{\alpha} (m_p l_p^2 + J_p) - \alpha_t g l_p m_p - l_p m_p r \ddot{\theta} &= 0 \end{aligned} \quad (1.22)$$

We can then rewrite this dynamical system in state space form:

$$\begin{aligned} \dot{x} &= Ax + Bu \\ y &= Cx + Du \end{aligned} \quad (1.23)$$

Where  $x$  is the state vector,  $y$  is the output vector and  $u$  is the input (or control) vector, that we expressed as:

$$\begin{aligned} x^T &= [\theta \ \alpha \ \dot{\theta} \ \dot{\alpha}] \\ y^T &= [\theta \ \alpha] \\ u &= V_m \end{aligned} \quad (1.24)$$

Finally, the corresponding  $A, B, C$  and  $D$  matrices are:

$$A = \begin{bmatrix} 0 & 0 & 1 & 0 \\ 0 & 0 & 0 & 1 \\ 0 & \frac{g l_p^2 m_p^2 r}{J_T} & -\frac{(m_p l_p^2 + J_p) \eta_g \eta_m k_m k_t K_g^2 + B_r R_m}{J_T R_m} & -\frac{B_p l_p m_p r}{J_T} \\ 0 & \frac{g l_p m_p m_p r^2 + J_a}{J_T} & -\frac{l_p m_p r \eta_g \eta_m k_m k_t K_g^2 + B_r R_m}{J_T R_m} & -\frac{B_p m_p r^2 + J_a}{J_T} \end{bmatrix} \quad (1.25)$$

$$B = \begin{bmatrix} 0 \\ 0 \\ \frac{K_g \eta_g \eta_m k_t (m_p l_p^2 + J_p)}{J_T R_m} \\ \frac{K_g \eta_g \eta_m k_t l_p m_p r}{J_T R_m} \end{bmatrix} \quad C = \begin{bmatrix} 1 & 0 & 0 & 0 \\ 0 & 1 & 0 & 0 \end{bmatrix} \quad D = \begin{bmatrix} 0 \\ 0 \end{bmatrix}$$

Where:

$$J_T = J_a m_p l_p^2 + J_p m_p r^2 + J_a J_p \quad (1.26)$$

### 1.3.2 Stable Equilibrium

To linearize around the stable position the steps are the same of the previous section, in this case the equilibrium position is:

$$z_0 = [0; \pi; 0; 0; 0; 0] \quad (1.27)$$

Now the corresponding linearized equations of motion are:

$$\begin{aligned} B_r \dot{\theta} + \ddot{\theta} (m_p r^2 + J_a) + \ddot{\alpha} l_p m_p r &= \tau \\ B_p \dot{\alpha} + \ddot{\alpha} (m_p l_p^2 + J_p) + \alpha_t g l_p m_p + l_p m_p r \ddot{\theta} &= 0 \end{aligned} \quad (1.28)$$

For these equations, A, B, C, D matrices are similar to the once reported in Eq. 1.25.

## 1.4 Simulation and Experiments

### 1.4.1 Description of Experiment and Results

To verify the accuracy of our model and its ability to explain real-world behavior, we conducted experiments using different input voltages. For each experiment, we compared our simulated results with actual measurements of  $\alpha$  and  $\theta$ .

It's important to note that the input voltage was applied in the downward configuration. Choosing a limited amplitude and duration of the input allowed us to use the linearized model.

Focusing on one specific experiment characterized by an impulsive input voltage with an amplitude of 2 [V] and a duration time of 0.1 [s].

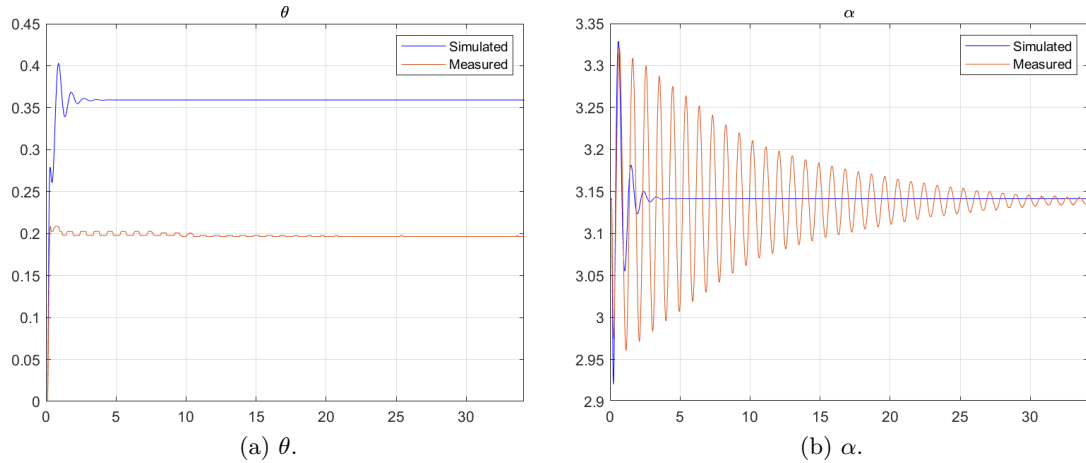


Figure 1.2: Simulated and Measured Angles  $\theta$  and  $\alpha$ .

If we look at Figure 1.2, the simulated system accurately captures the initial behavior of the real mechanism. However, some significant over-damping on  $\alpha$  and a meaningful overshoot on  $\theta$  differentiate it with respect to the real behaviour.

This outcome was consistent across all experiments, regardless of the magnitude of variation in  $\alpha$ , whether linearized or nonlinear.

### 1.4.2 Operative Notes

$\theta$  and  $\alpha$  are measured with two encoders with a resolution of 4096 counts per revolution. To transform this measure in radians it is multiplied by a gain of  $\frac{2\pi}{4096}$ . Being the pendulum starting in the stable position, in order to have the measure of  $\alpha$  aligned with the reference system that we used in the modelling, an offset of  $\pi$  is been added.

We also notice that, when a positive voltage is applied to the motor, its response is characterized by a clockwise rotation, which is different from the sign convection used in the modelling. To solve this problem a simple gain of  $-1$  is added in the *SIMULINK* and this allows to obtain a correlation between positive input voltage and a counter clockwise movement of the horizontal arm.

Finally, it is worth mentioning that for all simulations, a fixed-step, first-order solver named *ode1* was employed, with a sampling time of  $T_s = 2 \text{ ms}$ . However, during the experimental validation we alternated between  $T_s = 2 \text{ ms}$  and  $T_s = 1 \text{ ms}$ . This adjustment in the sampling time was necessary to address the hardware-related challenges encountered with the setup.

## 2. System Identification

The utilization of nominal parameters led to an over-damped response of the system, as demonstrated in the preceding chapter. Therefore, it became essential to employ a system identification procedure. The primary objective of this process is to estimate the set of parameters  $\mathbf{x}$  that characterize the dynamic model of interest using a collection of experimental data.

During the modeling phase, we leveraged the *MATLAB symbolic math toolbox* to facilitate the derivation of the nonlinear equations of motion. Consequently, we chose to employ a grey-box system identification procedure utilizing the "Simulation Error Method" (S.E.M.). This identification routine entails solving a nonlinear, constrained, least-squares optimization problem and offers various advantages, including:

- The ability to incorporate constraints on both the state variables and parameters, allowing us to integrate relevant physical knowledge about the system
- Leveraging the non linear model to simulate the system multiple steps ahead
- Obtaining a more accurate estimated model, as a model with lower simulation error is less susceptible to issues associated with fast sampling and significant measurement noise

### 2.1 Identification of the Non Linear Model of the Rotary Inverted Pendulum

To begin with, we extracted the parameters with the highest uncertainty from the provided data sheets [5] and selected them as the optimization variables. These parameters, along with their nominal values and associated uncertainties, are listed in Table 2.1. Furthermore, we also determined the moments of inertia  $J_p$  and  $J_a$ , as well as the viscous damping coefficients  $B_p$  and  $B_r$ , even though no specific uncertainties were provided for these variables.

To establish constraints for our optimization problem, we defined inequalities that the solution must satisfy. This allowed us to define the allowable range of variation for the physical parameters. For parameters with known uncertainties, the interval was defined as follows:

$$x \in [x_{nom} - x_{nom} \times Uncertainty(\%), x_{nom} + x_{nom} \times Uncertainty(\%)] \quad (2.1)$$

For parameters that did not have specified uncertainties, we determined arbitrary upper and lower bounds. The comprehensive set of constraints can be found in the appendix in Eq. A1.

The objective of our optimization problem was to minimize the cost function at each iteration. The cost function was defined as follows:

$$\begin{aligned} & \underset{\mathbf{x}}{\text{minimize}} \quad \frac{1}{N} \sum_{i=0}^N (\tilde{\mathbf{y}}(i) - \hat{\mathbf{y}}(i))^2 \\ & \text{subject to} \quad \hat{\mathbf{z}}(i+1) = f_{\mathbf{z}}(\hat{\mathbf{z}}(i), \tilde{\mathbf{u}}(i), \mathbf{x}), \quad i = 1, \dots, N. \\ & \quad \hat{\mathbf{y}}(i) = \hat{\mathbf{z}}(i), \quad i = 0, \dots, N. \\ & \quad \hat{\mathbf{z}}(0) = \tilde{\mathbf{z}}(0) \\ & \quad C\mathbf{x} \geq \mathbf{d} \end{aligned} \quad (2.2)$$

where  $\tilde{\mathbf{y}}(i) = (\tilde{\theta}(i), \tilde{\alpha}(i))^T$  is the  $i^{th}$  sample from encoders measurements, while  $\hat{\mathbf{y}}(i) = (\hat{\theta}(i), \hat{\alpha}(i))^T$  is the estimated output at step  $i^{th}$  through the simulation of the non linear model  $f_{\mathbf{z}}(\mathbf{z}, \tilde{\mathbf{u}}, \mathbf{x})$  of the pendulum over  $N$  steps.  $\mathbf{x}$  denotes the current parameters values,  $\mathbf{z}$  denotes the state vector,  $\tilde{\mathbf{u}}$  is the measured input voltage  $V_m$ ,  $C\mathbf{x} \geq \mathbf{d}$  contains the 20 linear inequality constraints mentioned earlier. Since the cost function comprises squared fitting errors and the parameter constraints are linear, we can effectively solve the problem using Sequential Quadratic Programming (SQP) approaches. In our

case, we employed a constrained Gauss-Newton technique, which resulted in the parameter estimates presented in Table 2.1.

	<b>Identified Value</b>	<b>Nominal Value</b>	<b>Uncertainty</b>	<b>Units</b>
$J_a$	$1 \times 10^{-4}$	$2 \times 10^{-3}$	—	$kg \times m^2$
$J_p$	$8 \times 10^{-4}$	$1.2 \times 10^{-2}$	—	$kg \times m^2$
$l_p$	$2.92 \times 10^{-2}$	$1.56 \times 10^{-1}$	—	$m$
$B_r$	$2.1 \times 10^{-3}$	$2.4 \times 10^{-3}$	—	$Nms/rad$
$B_p$	$4 \times 10^{-4}$	$2.4 \times 10^{-3}$	—	$Nms/rad$
$\eta_g$	$9.339 \times 10^{-1}$	$9.0 \times 10^{-1}$	$\pm 10\%$	
$\eta_m$	$7.077 \times 10^{-1}$	$6.9 \times 10^{-1}$	$\pm 5\%$	
$k_t$	$7.4 \times 10^{-3}$	$7.68 \times 10^{-3}$	$\pm 12\%$	$Nm/A$
$k_m$	$8.5 \times 10^{-3}$	$7.68 \times 10^{-3}$	$\pm 12\%$	$V/(rad/s)$
$R_m$	2.3834	2.6	$\pm 12\%$	$\Omega$

Table 2.1: Identified Parameters

### 2.1.1 Training Set

As a training data-set we used an input voltage signal made of 3 impulsive excitations of the duration of around 0.1 [s] and with a variable amplitude between 2[V] and 3[V].

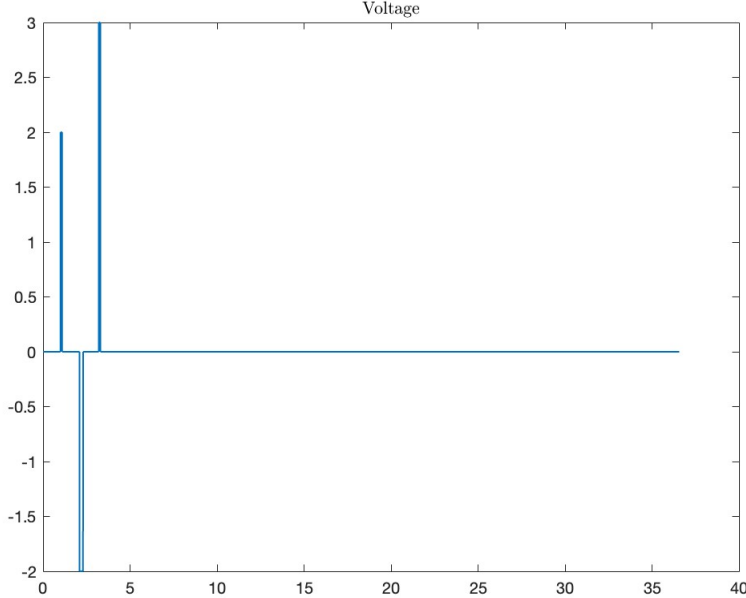


Figure 2.1: Input Voltage for Training.

The results of the identification procedure on the training set, provided a goodness of fit of 68.7% on  $\theta$  and 82.97% over  $\alpha$ .

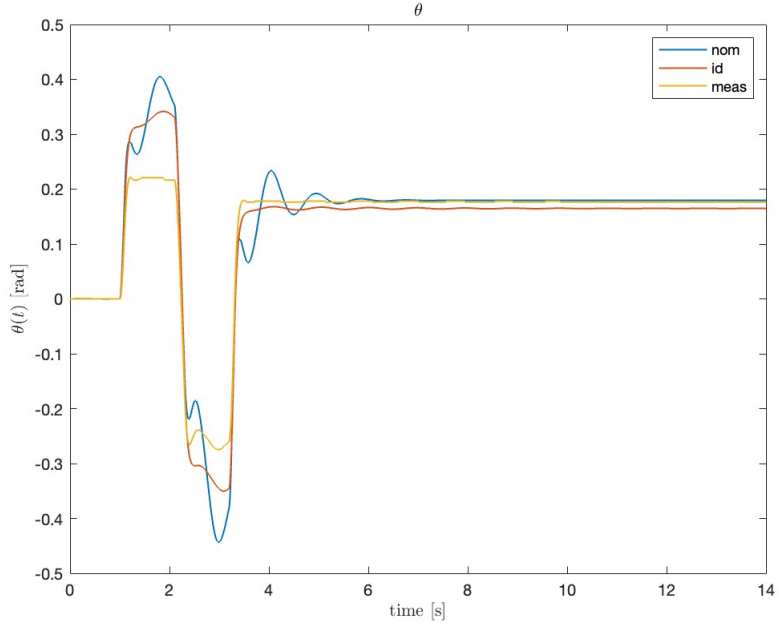


Figure 2.2:  $\theta$  Angle in Training.

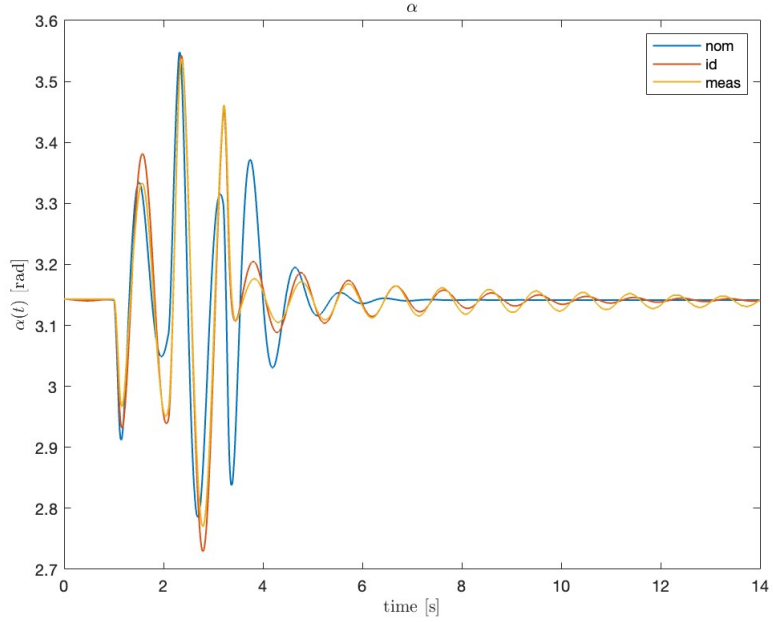


Figure 2.3:  $\alpha$  Angle in Training.

From Figure 2.2, it is evident that the simulated model exhibits overshoots and settles to a lower value compared to the real experimental data. This behavior can be attributed to two main reasons:

- The cable powering and transmitting the encoder signal on the pendulum joint may introduce minor and unmodeled oscillations.
- The unmodeled static friction affecting the gears can significantly impact the premature cessation of arm rotation.

These factors ultimately influence the real evolution of the angle alpha as well, as depicted in Figure 2.3. It is notable that the real alpha exhibits greater oscillations compared to the simulated counterpart.

### 2.1.2 Validation Set

For the validation set, we applied a simple impulse voltage with a duration of 0.1 [s] and a magnitude of 10 [V]. This specific input signal was chosen for validation purposes due to the unsatisfactory response achieved in simulation with the nominal model.

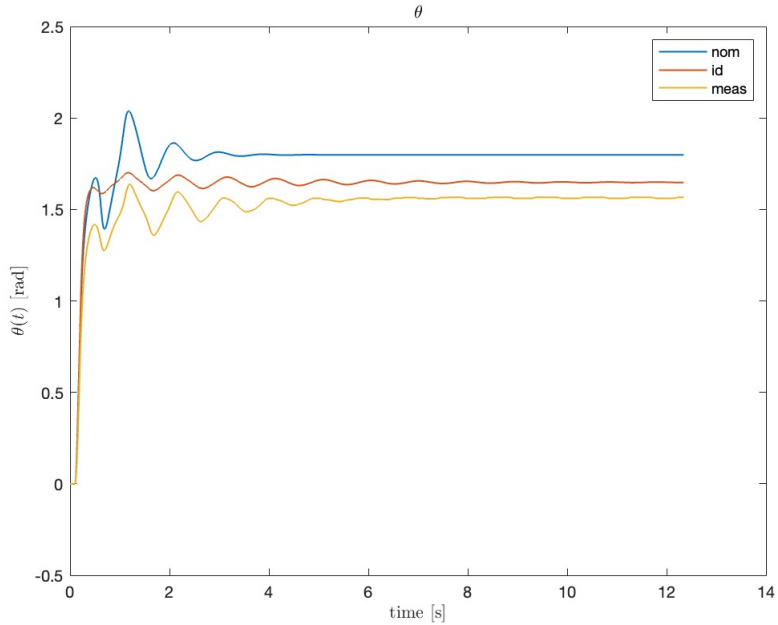


Figure 2.4:  $\theta$  Angle in Validation.

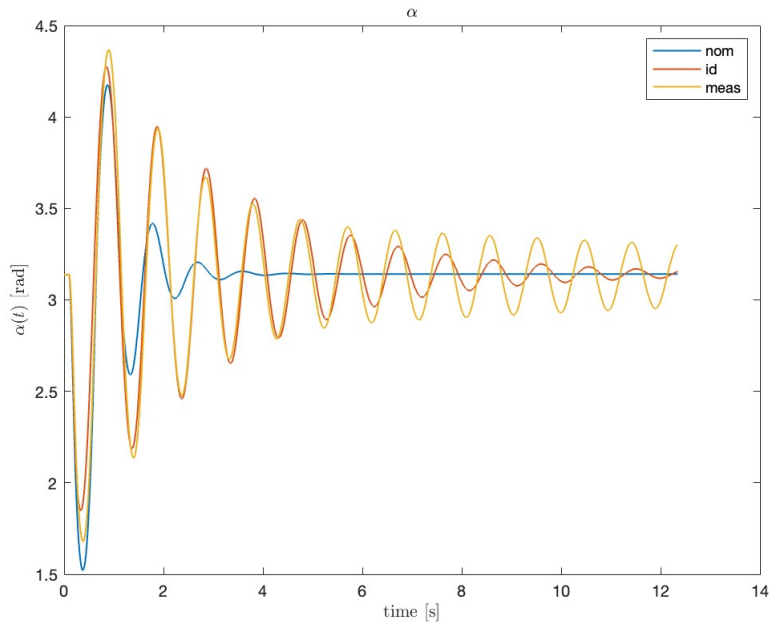


Figure 2.5:  $\alpha$  Angle in Validation.

The performance on the validation set is generally satisfactory, particularly in simulating the behavior of the  $\alpha$  angle, where the goodness of fit reaches 67.61%. However, for the  $\theta$  angle, the performance is lower, with a goodness of fit of only 37.99%. This lower performance can be attributed primarily to the influence of static friction. The quantitative assessment of the improvements achieved through the identification procedure can be found in Table 2.2.

	<b>Nominal <math>\theta</math> %</b>	<b>Identified <math>\theta</math> %</b>	<b>Nominal <math>\alpha</math> %</b>	<b>Identified <math>\alpha</math> %</b>
Training	60.74	68.7	23.94	82.97
Validation	-29.46	37.99	40.85	67.61
Chirp	-39.15	-27.06	58.24	-17.22

Table 2.2: Comparison of fit % in Time Domain.

As a side note, the goodness of fit for both training and validation experiments is computed as reported in [3]. The equation is provided in the appendix, as Eq. A2.

### 2.1.3 Frequency Domain Validation and Chirp Signal

To comprehensively evaluate the results of the identification procedure, a frequency domain analysis was performed. A chirp voltage signal was applied to the DC motor to excite a wide range of frequencies. Figure 2.6 displays the achieved frequency range, ranging from nearly 0 [Hz] up to 12 [Hz]. This frequency range is considered sufficient since the low natural frequency of our system typically falls below 10 [rad/s].

Subsequently, the same input voltage was used to simulate both the nominal and identified nonlinear models of the pendulum. The magnitude of the Bode diagram was computed for both  $\theta$  and  $\alpha$  using experimental data and simulations.

$$|G(j\omega)| = \frac{|Y(j\omega)|}{|U(j\omega)|} \quad (2.3)$$

In Figures 2.7 and Figures 2.8, the superiority of the identified model over the nominal one is evident in the higher frequency range of the spectrum. However, significant inconsistencies arise at lower frequencies in the bode diagram of  $\alpha$ , where the nominal model appears to align more accurately with the experimental data. Regarding the resonant peak, the orange curve tends to overestimate the experimental value, whereas the nominal model underestimates it.

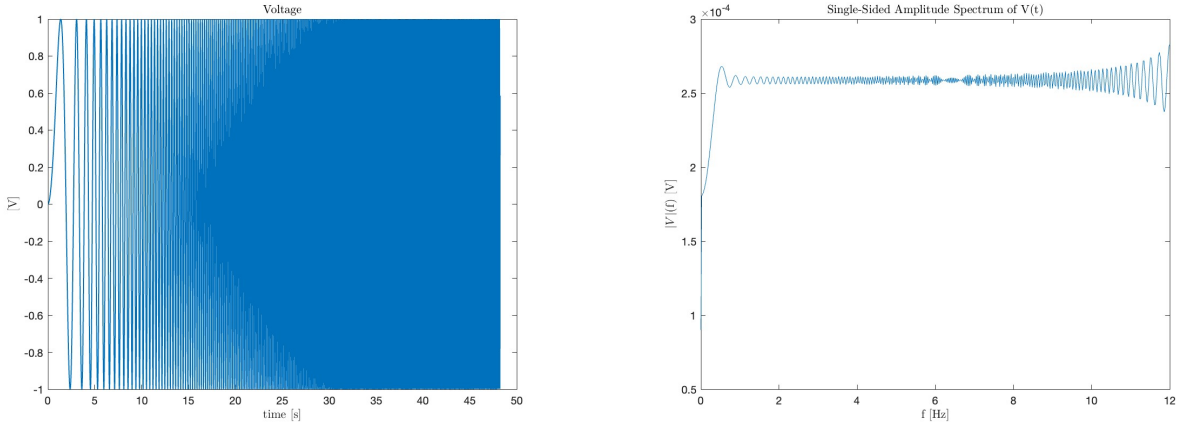


Figure 2.6: Chirp Input Voltage.

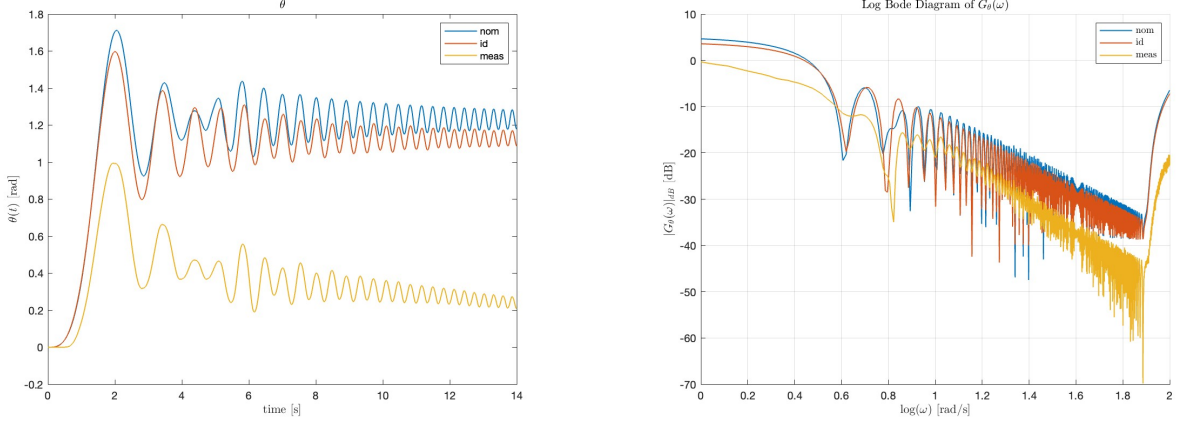


Figure 2.7: Chirp  $\theta$ .

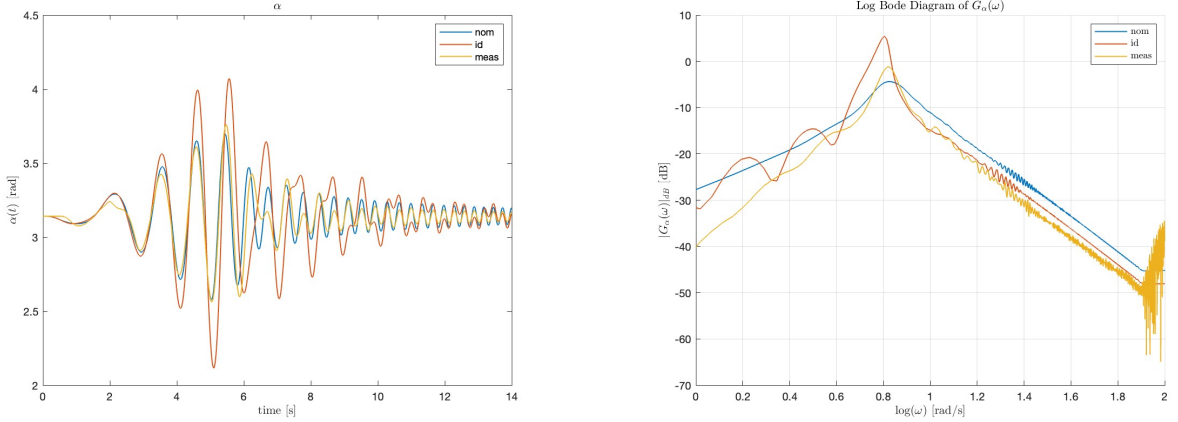


Figure 2.8: Chirp  $\alpha$ .

	<b>Nominal <math>\theta</math></b>	<b>Identified <math>\theta</math></b>	<b>Nominal <math>\alpha</math></b>	<b>Identified <math>\alpha</math></b>
Training	$3.49 \times 10^{-10}$	$2.79 \times 10^{-10}$	$2.8 \times 10^{-10}$	$3.48 \times 10^{-11}$
Validation	$6.99 \times 10^{-8}$	$1.54 \times 10^{-8}$	$8.21 \times 10^{-8}$	$2.04 \times 10^{-8}$
Chirp	$3.41 \times 10^{-9}$	$2.58 \times 10^{-9}$	$3.94 \times 10^{-10}$	$3.6 \times 10^{-9}$

Table 2.3: Comparison of M.S.E. in Frequency Domain.

	<b>Id. [dB]</b>	<b>Id. [rad/s]</b>	<b>Nom. [dB]</b>	<b>Nom. [rad/s]</b>	<b>Exp. [dB]</b>	<b>Exp. [rad/s]</b>
Training	10.72	6.30	-2.06	6.30	11.56	6.30
Validation	5.43	6.60	-0.667	6.60	8.086	6.60
Chirp	5.41	6.02	-4.37	6.60	-1.15	6.60

Table 2.4:  $\alpha$  Resonance Peaks Magnitude and Frequency.

Table 2.3 shows that the Mean Squared Error (MSE) on  $\alpha$  for the chirp experiment is lower for the nominal model compared to the identified one. This pattern is also evident from the time domain analysis in Figure 2.8.

Furthermore, Table 2.4 provides a comparison of the characteristics of the peaks in the bode diagrams for all mentioned experiments. It can be observed that the resonant frequency is generally well-matched

by both the nominal and identified models. However, when it comes to impulsive-like excitations, the identified model consistently outperforms the nominal one. On the other hand, for chirp signals, the evolution of the pendulum angle is described more faithfully by the nominal model.

#### 2.1.4 Residual Analysis

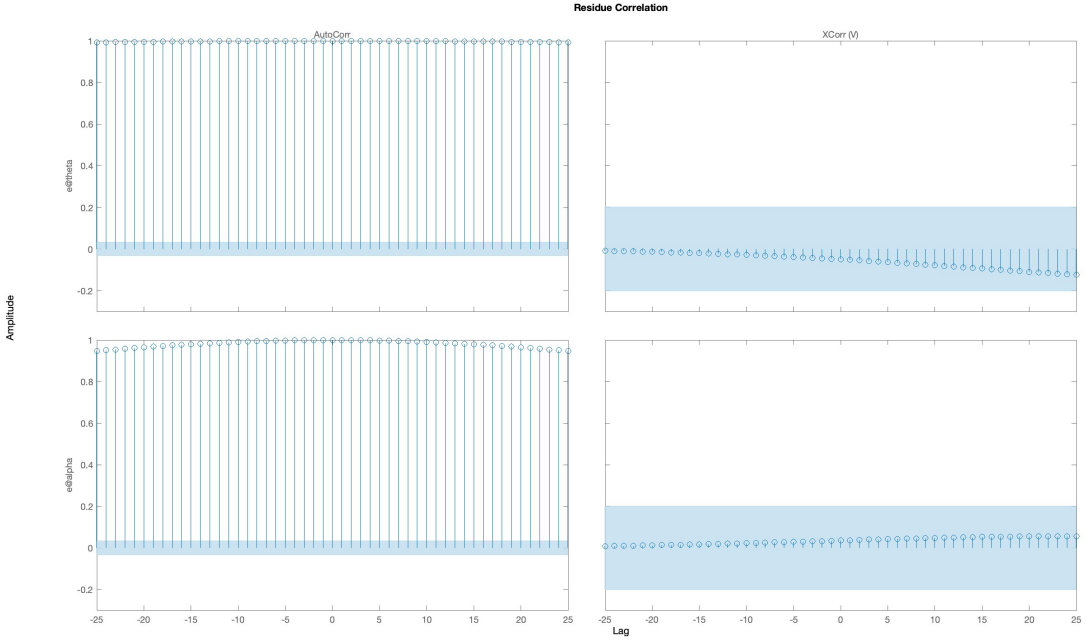


Figure 2.9: Residual Analysis.

The residual analysis performed on the validation dataset provides valuable insights. It indicates that the identified parameters yield a nonlinear model with high auto-correlation for both  $\theta$  and  $\alpha$ , while showing low correlation with the input signal. This suggests that the model effectively captures the intrinsic dynamics of the system but fails to account for unmodeled behavior in the disturbance path. This finding aligns with the omission of the disturbance during the modeling phase. To enhance the model's accuracy, a more accurate approach would involve incorporating a disturbance model. By incorporating a model for the disturbance, it becomes possible to reduce the auto-correlation within the confidence interval bounds, resulting in a more accurate representation of the system's behavior.

### 3. Frequency Based Control

The objective of this chapter is to regulate the position of the horizontal arm by manipulating the voltage applied to the motor. To achieve this, a frequency-based strategy is employed, leveraging the parameters identified in Chapter 2.

#### 3.1 Open Loop Analysis

To begin, we initiate an analysis of the system in an open-loop configuration. Starting from the state space representation in the stable equilibrium position, four transfer functions are computed. These transfer functions have the motor voltage as their input and the following four states as their outputs:  $\theta$ ,  $\alpha$ ,  $\dot{\theta}$ , and  $\dot{\alpha}$ . For the purpose of position control of the horizontal arm, our primary focus lies on the first transfer function:

$$G_{V\theta}(s) = 27.22 \frac{s^2 + 0.46 s + 42.42}{s(s + 16.25)(s^2 + 0.79 s + 43.12)} \quad (3.1)$$

The transfer function of interest for position control of the horizontal arm has an order of four. It is characterized by two complex and conjugate zeros, along with four poles: one real, two complex and conjugate, and one at the origin.

$$\begin{aligned} Poles &= [0 \ -16.25 \ -0.39 + 6.55i \ -0.39 - 6.55i] \\ Zeros &= [-0.23 - 6.51i \ -0.23 + 6.51i] \end{aligned} \quad (3.2)$$

As a result of the integral action, the DC gain of the transfer function becomes infinite. Consequently, if a step input voltage is applied to the motor, the angular position  $\theta$  will continue to increase indefinitely. However, the transfer function from motor voltage to angular speed  $\dot{\theta}$  exhibits a DC gain of  $1.65[\text{rad/s}]$ . Thus, with a step input at steady state,  $\dot{\theta}$  will remain constant, resulting in no acceleration. These details can be found in Table 3.1.

T.F.	DC Gain	Phase Margin	Crossover Freq.
$G_{V\theta}$	$\infty$	83.49	1.64
$G_{V\alpha}$	$2.14 \times 10^{-17}$	37.16	5.98
$G_{V\dot{\theta}}$	1.65	127.6	21.88
$G_{V\dot{\alpha}}$	$2.21 \times 10^{-16}$	-51.99	22.52

Table 3.1: Open Loop Properties.

Since the DC gain of Eq. 3.1 is infinite, it is not possible to determine the system's bandwidth directly from its Bode plot. However, we can derive the transfer function from motor voltage to angular velocity of the horizontal arm  $\dot{\theta}$ :

$$G_{V\dot{\theta}}(s) = 27.22 \frac{s^2 + 0.46 s + 42.42}{(s + 16.25)(s^2 + 0.79 s + 43.12)} \quad (3.3)$$

The bode plot of Eq. 3.3 is depicted in Figure 3.1.

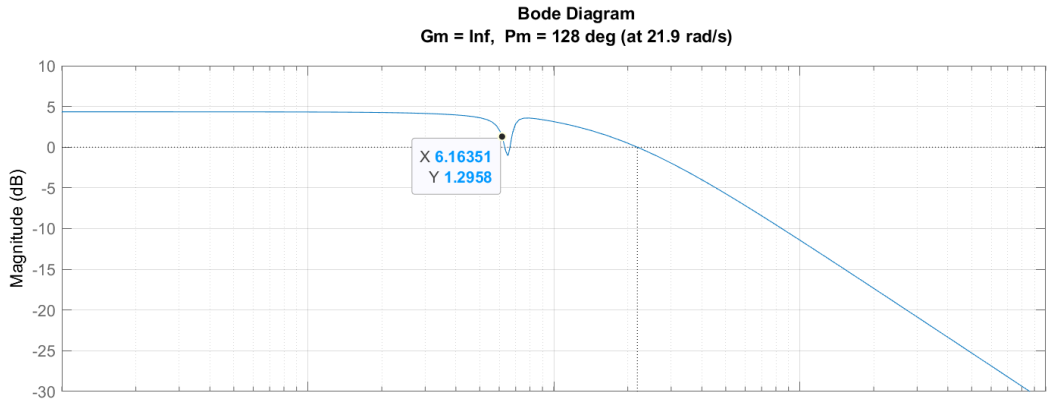


Figure 3.1: Bode Diagram of Eq. 3.3.

The bandwidth of the system is the frequency where the DC gain is reduced by 3 [dB]. This point is highlighted in the figure and corresponds to a frequency of 6.16 [rad/s].

## 3.2 Controller Design

The controller design for the system follows a loop-shaping approach. Initially, we observe that the transfer function  $G_{V\theta}(s)$  is asymptotically stable, allowing us to utilize the Bode criterion for stability analysis during the design phase. According to the Bode criterion, it is necessary for the gain of the loop transfer function  $L(s)$  to be strictly positive ( $\mu_L > 0$ ), the phase margin of  $L(s)$  to be strictly greater than zero ( $\phi_m > 0$ ), the Bode plot of  $L(s)$  to intersect the 0 [dB] axis only once, and the feedback connection to be negative (which can be generalized to positive feedbacks).

The design specifications that were formulated to meet the desired system performance are summarized in Table 3.4. Poles and zeros have been intentionally placed in the system to satisfy these requirements. Moreover, we considered acceptable only voltage input signals saturating for no more than 0.1 [s].

### 3.2.1 $L(s)$ Design

In order to achieve steady-state zero-error regulation for constant reference signals, our goal was to design a closed-loop system that behaves as a first-order system with integral action. As  $G_{V\theta}(s)$  is asymptotically stable, we proceeded by canceling out the complex conjugate poles and zeros of the system.

During this stage of the design, we observed that a first-order system alone placed excessive emphasis on the input voltage and did not meet our desired performance criteria. This could be attributed to imperfect cancellations of poles and zeros, as well as the presence of integral action. To address this, we introduced an additional pole to the design at a slightly higher frequency. The poles and zeros of the controller are listed in Table 3.2, and the transfer function of the controller is given by Eq. 3.4.

$$R(s) = 928.32 \frac{(s + 16.24)(s^2 + 0.793s + 43.11)}{(s + 58.62)(s + 44.73)(s^2 + 0.4579s + 42.42)} \quad (3.4)$$

Type	Location	Damping	Frequency
Real Zero	-16.2	1	16.2
Real Pole	-44.7	1	44.7
Real Pole	-58.6	1	58.6
Complex Zeros	$-0.397 \pm 6.55i$	0.0604	6.57
Complex Poles	$-0.229 \pm 6.51i$	0.0352	6.51

Table 3.2: Regulator  $R(s)$  Singularities.

### 3.2.2 Stability

By examining the Bode plot of  $L(s) = G_{V\theta}(s) \cdot R(s)$ , we can confirm that our design satisfies the conditions of the Bode Criterion. It is worth noting that the DC gain is infinite.

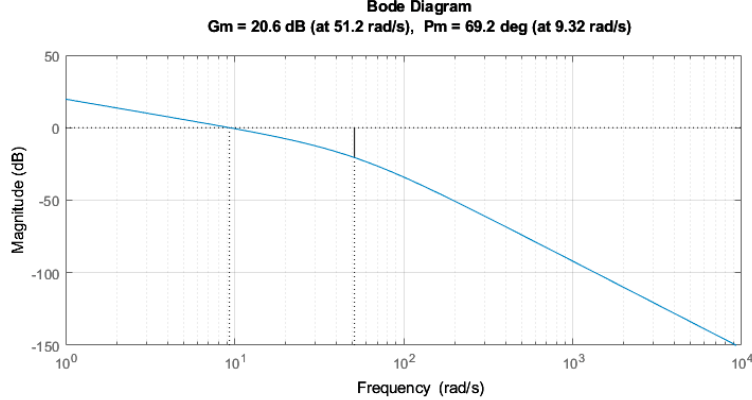


Figure 3.2: Bode Diagram of  $L(s)$ .

### 3.2.3 Performances: Sensitivity Functions

The closed-loop system shown in Figure 3.3a exhibits a complementary sensitivity function with a bandwidth of approximately 14.76 [rad/s], indicating a significant improvement in system speed. Additionally, the sensitivity function, as depicted in Figure 3.3b, has a cutoff frequency of around 11 [rad/s]. Furthermore, the control sensitivity function, shown in Figure 3.3c, demonstrates limited gain within the 14 [rad/s] frequency range. This characteristic ensures that the input voltage remains within the saturation constraints of the actuator, as illustrated in Figure 3.3d.

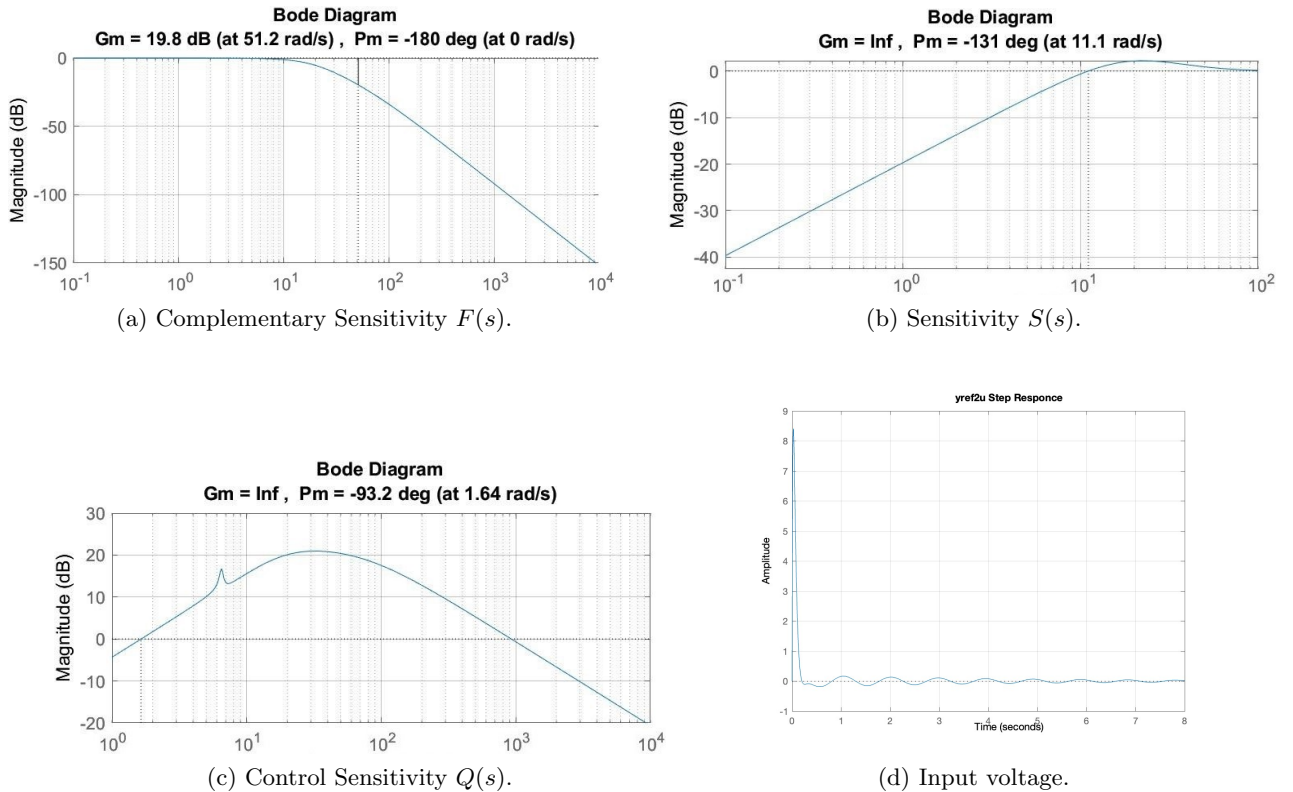


Figure 3.3: Sensitivity Functions.

	$\mathbf{F}(s)$	$\mathbf{S}(s)$	$\mathbf{Q}(s)$
$\omega_{peak} [rad/s]$	—	21.6	32
$\ \cdot\ _{peak} [dB]$	—	2.21	21
Bandwidth [rad/s]	14.76	7.18	—

Table 3.3: Peaks and Bandwidths.

### 3.2.4 Behaviour of Alpha $G_{Y\alpha}(s)$ in the Closed-Loop System

The block diagram in Figure 3.4 illustrates the adopted control scheme.

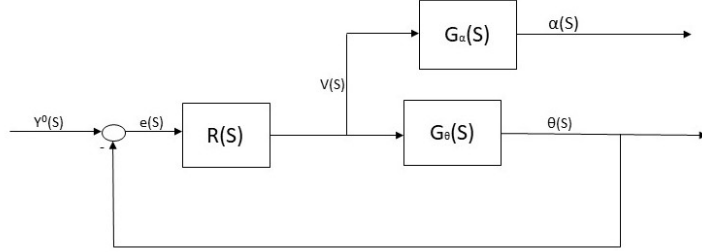


Figure 3.4: Frequency Based Control Scheme.

In order to gain insights into the behavior of  $\alpha$  when the controller on  $\theta$  is active, we examined the transfer function  $G_{Y\alpha}(s)$ , which describes the relationship between  $\alpha(s)$  and the reference  $Y^0(s)$  in the closed-loop system. The transfer function is derived as follows:

$$G_{Y\alpha}(s) = \frac{\alpha(s)}{Y^0(s)} = \frac{R(s) G_\alpha(s)}{1 + R(s) G_\theta(s)} = \frac{R(s) G_\alpha(s)}{1 + L_\theta(s)} = Q_\theta(s) G_\alpha(s) \quad (3.5)$$

Analyzing the Bode plot of  $G_{Y\alpha}(s)$ , we observe the presence of a resonance peak around 6.54 [rad/s]. Through experimental verification, we found that exciting the system near this frequency leads to poor performance of the closed-loop system.

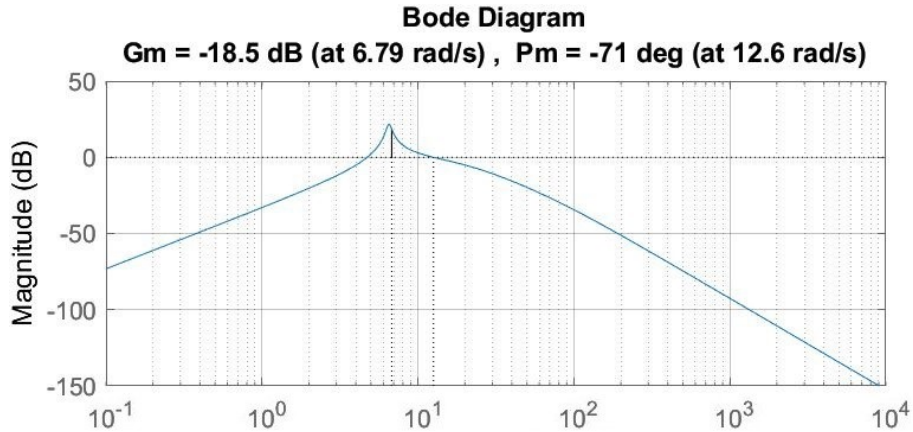


Figure 3.5:  $G_{Y\alpha}(s)$ .

## 3.3 Performances: Step Response

The unit step response yielded the following results. It is evident that both the linear and non-linear models satisfy the given specifications.

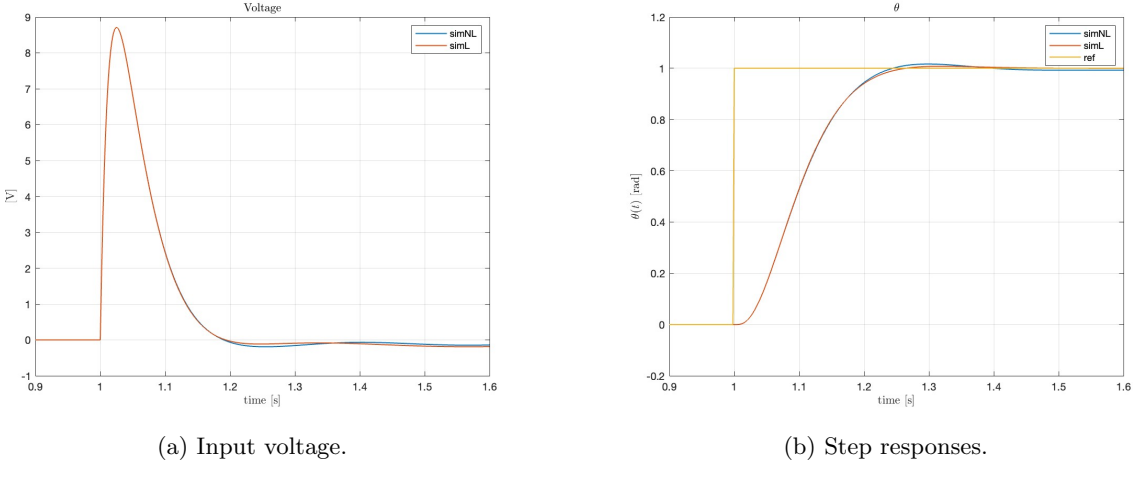


Figure 3.6: Step Response Performances.

	Specifications	Linear Model	Non Linear Model
Rise Time [s]	$\leq 0.2$	0.141	0.140
Settling Time [s]	$\leq 0.3 s$	0.231	0.223
Overshoot $O_{sh}$ (%)	5 %	0.76 %	1.65 %
Peak Time [s]	/	0.319	0.298
Voltage	10[V] for max. 0.1[s]	/	/

Table 3.4: Specifications and Simulation of the Unitary Step.

### 3.4 Experiment

After confirming that the specifications were met in simulation for both the linear and non-linear models during a unit step response, we proceeded to implement the controller on the physical system. Table 3.5 provides a summary of the comparison between simulation and experimental results.

To test the controller we performed different experiments, with different reference signals for the horizontal arm angle  $\theta$ . In the next figure there is the result obtained by feeding the controller with a square wave (more critical situation with respect to a sinusoidal wave) as reference of  $\theta$ , with an amplitude of 0.52 [rad] and a frequency of 0.5 [Hz]:

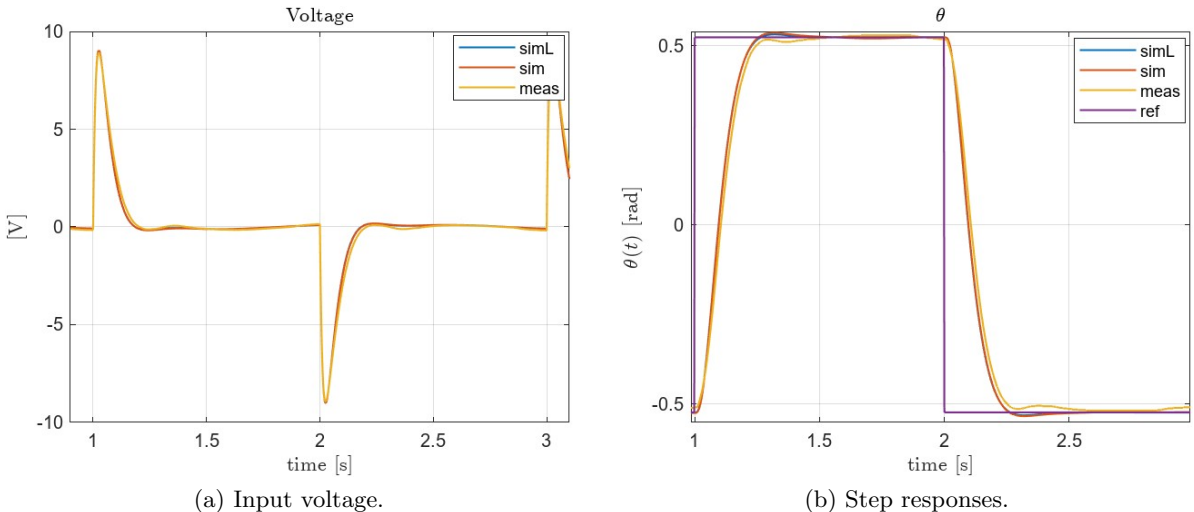


Figure 3.7: Experimental Square Wave Response.

	<b>Measured Results</b>	<b>Linear Model</b>	<b>Non Linear Model</b>
Rise Time [s]	0.145	0.135	0.133
Settling Time [s]	0.253	0.232	0.229
Overshoot $O_{sh}$ (%)	0.992%	0.76%	1.16%
Peak Time [s]	0.666	0.320	0.318
Voltage max. [V]	8.92	9.03	9.04

Table 3.5: Experimental and Simulated Results of the Closed Loop System.

### 3.4.1 Experimental Behaviour of $G_{Y\alpha}(s)$ : Resonance

By applying a square wave reference signal with an amplitude of 0.1 [rad] at the resonant frequency of 6.54 [rad/s] as illustrated in Figure 3.5, substantial displacements of  $\alpha$  from the downward configuration are observed, providing empirical validation of the previously conducted simulations. A precise position control of the horizontal arm becomes particularly challenging in the around of these frequencies.

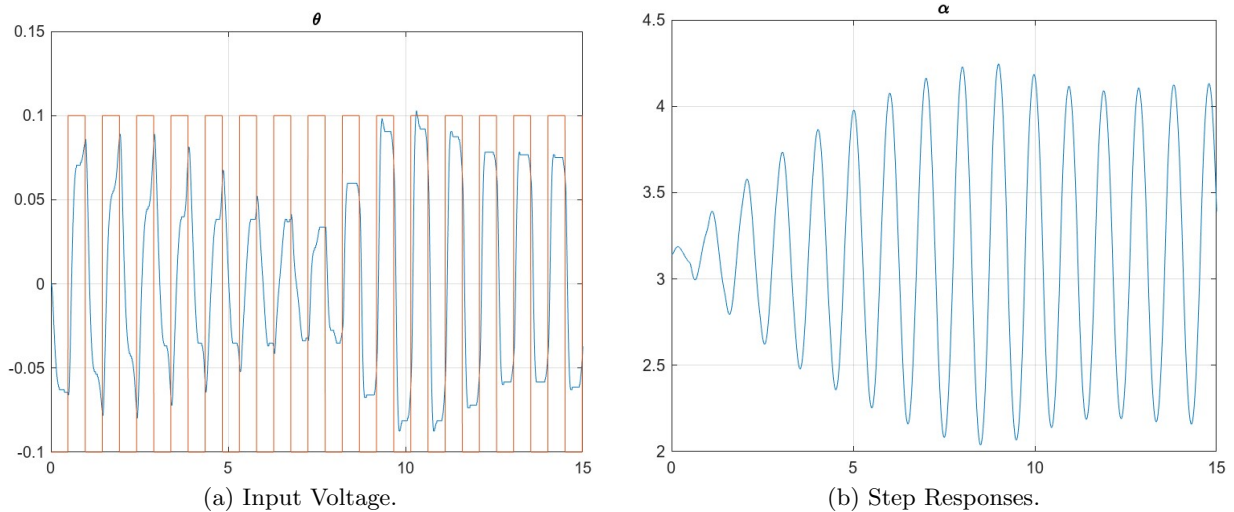


Figure 3.8: Resonance of  $G_{Y\alpha}(s)$ .

## 4. State Space Based Control

To stabilize the pendulum in the upright position, two control strategies have been adopted: Pole Placement and Linear Quadratic Gaussian control (LQG). Both designs aim to first stabilize the pendulum and then track a reference for  $\theta$  while maintaining the pendulum in the unstable equilibrium.

The controller designs are simulated using full state feedback and then tested with velocity estimates obtained from either a Luenberger observer or a Kalman filter. The inputs provided to the controller consist of a combination of measurements and estimates: the measurements of  $\theta$  and  $\alpha$ , and the estimates of  $\dot{\theta}$  and  $\dot{\alpha}$ .

The controllers must satisfy the following specifications:

- $e_\infty = 0$
- Settling time  $t_s \leq 1.5$  [s] for the worst initial condition of  $\alpha$
- Voltage saturation limited to a maximum of 0.1 [s] with input saturation occurring at  $\pm 10$  [V]

While evaluating the performance of the observer (and the Kalman filter) in simulations, we focused on the estimation of  $\dot{\alpha}$  and  $\hat{\alpha}$ . In experimental testing, the performance is assessed only for  $\alpha$  since  $\dot{\alpha}$  measurements are not available, and  $\theta$  does not pose any difficulties. The initial conditions for the observers are always set at the equilibrium.

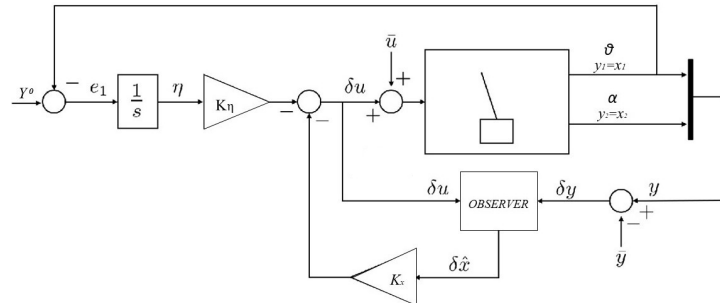


Figure 4.1: General Control Scheme for a State Space Controller.

### 4.1 Pole Placement Controller

Our objective in this control design is to optimize for the fastest achievable stabilizing controller, considering the limitations imposed by the actuator capabilities, and not placing excessive emphasis on robustness considerations.

Analyzing the system in its state space representation around the unstable equilibrium, Eq. 1.25, we obtain the pole values:  $\{0; 6.41; -6.42; -17.02\}$ .

The presence of a pole with a positive real part makes the equilibrium unstable, while the pole at the origin represents a pure integral action.

To design a Pole Placement controller capable of stabilizing the pendulum in the vertical position, we assumed that all states of the system were measurable. During the experimental verification, the full state feedback is achieved through the estimation of the velocities  $\dot{\theta}$  and  $\dot{\alpha}$  using measurements from the encoders.

Before selecting the pole positions, we verified that the pair  $(A, B)$  is reachable, being the  $\text{rank}(M_r)$  equal to  $\text{rank}(A)$ .

Starting from the following approximation of complex conjugates poles:  $\lambda_{1,2} = -\zeta\omega_n \pm i\omega_n$ , we place two dominant poles with  $\zeta = 0.7$  in order to reduce both overshoots and rise times. Introducing a pair of complex and conjugate poles with bounded imaginary part leads to a fast controller without stressing the actuator significantly or introducing excessive oscillations or noise amplification.

The poles positions have been tuned in the simulation to the following values:  
 $\{-8.4 + i12; -8.4 - i12; -11; -11\}$ .

It is important to note that the real part of the poles must be bounded to avoid input voltage saturation beyond the allowed limits.

With this configuration, the Pole Placement gain, obtained using the 'place' command in MATLAB, is the following horizontal vector:

$$K_{pp} = [-22.49 \quad 56.7 \quad -6.7 \quad 8.03] \quad (4.1)$$

Simulating the system with this controller using the nonlinear model produces the following results:

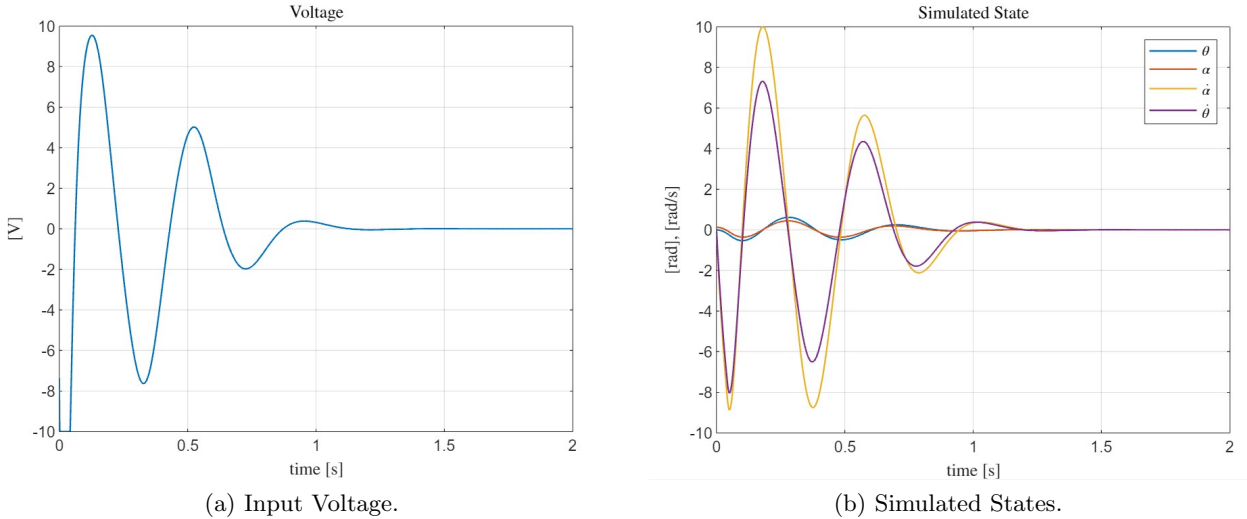


Figure 4.2: Pole Placement Controller in Simulation.

This simulation was performed with the worst initial condition for  $\alpha$  ( $0.13[\text{rad}]$ ) that the controller can stabilize. Even under such a condition, the design specifications are satisfied, specifically:

$\theta_{ts}=1.5$	$\alpha_{ts}=1.5$	$\dot{\theta}_{ts}=1.5$	$\dot{\alpha}_{ts}=1.5$	$\Delta t_{10}[\text{V}]$	$t_s$	$e_\infty$
$-5.71 \times 10^{-4}$	$-5.01 \times 10^{-4}$	$3.64 \times 10^{-3}$	$7.73 \times 10^{-3}$	0.04 [s]	1.3 [s]	0

Table 4.1: Simulation Data.

The settling time is defined as the time at which the value of  $\alpha$  reaches  $\pm 2.6 \times 10^{-3}$ . This value is computed using the definition in the Table 5.7. Although we cannot perform this check for the other states since they all start from zero, Table 4.1 shows that they are sufficiently low at  $1.5[\text{s}]$ , which is the maximum settling time that satisfies the specifications. In the initial conditions, we use  $\theta = 0$ , but any angle can be chosen as an equilibrium point and the initial velocities are set to 0 as well.

While testing  $K_{pp}$  in simulation is possible using full state feedback, this approach cannot be implemented on the real set-up. To execute the controller, we need to estimate the velocities based on the measurement of the angular positions  $\theta$  and  $\alpha$ . The first estimation method consisted in a simple derivative action and a low-pass filter with a cutoff frequency of  $\omega_0 = 125[\text{Hz}]$ , corresponding to the transfer function  $t.f. = \frac{s}{1+\frac{s}{125}}$ . However, this method amplifies noise and degrades performance. To achieve better results, we designed a Luenberger observer.

## 4.2 Luenberger Observer

Being the system completely observable, a full-order observer is designed to estimate the angular velocities,  $\hat{\theta}$  and  $\hat{\alpha}$ . This algorithm takes measurements of  $\theta$ ,  $\alpha$ , and the voltage applied to the system as inputs.

In the laboratory, we determined the desired observer poles as  $\{-40-i4, -40+i4, -50+i5, -50-i5\}$ . The use of complex conjugate poles results in a faster observer and thus reducing both the observer's inverse response and the unwanted oscillations of the horizontal arm at steady state.

We found experimentally that the performances were better by setting the imaginary part of the poles to  $1/10$  of the real part.

The ratio between the real part of the observer's dominant pole and the Pole Placement is  $\frac{-40}{-8.4} = 4.76$ . This indicates that the observer dynamic is sufficiently faster than the Pole Placement controller, while avoiding amplification of the noise at high frequencies.

The observer matrices are computed using the following code:

$$\begin{aligned} L_{obs} &= \text{place}(A', C', \text{obsv\_poles})'; & C_{ob} &= \text{eye}(n); \\ A_{ob} &= A - L_{obs} * C; & D_{ob} &= \text{zeros}(n, m + p); \\ B_{ob} &= [B - L_{obs} * D, L_{obs}]; \end{aligned}$$

Here, A, B, C, and D are the matrices from Eq. 1.25. The system order is  $n = 4$ , the input dimension is  $m = 1$ , and the measured output dimension is  $p = 2$ . For the simulation of the linearized observer, initial conditions are set to zero. The simulation results are the following:

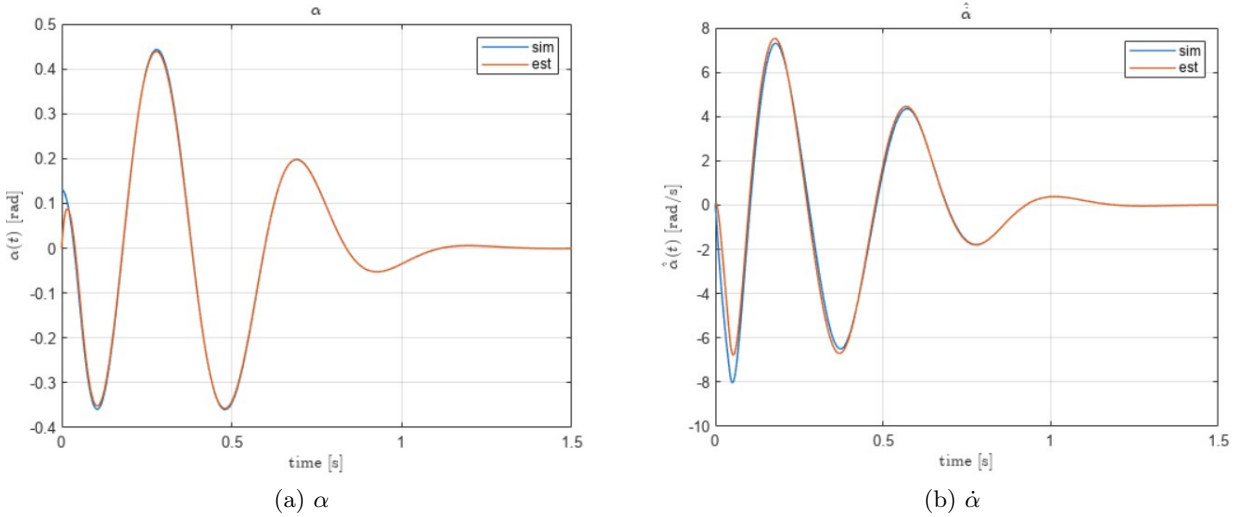


Figure 4.3: Luenberger Observer Simulation and Estimation.

The figure demonstrates the observer's performance in estimating  $\hat{\alpha}$  and  $\hat{\dot{\alpha}}$ . The initial error, resulting from the difference between the worst initial condition for  $\alpha$  and zero initial condition for the observer, is  $0.13 \text{ [rad]}$ . The estimated  $\hat{\alpha}$  intersects with the simulated line at  $0.02 \text{ [s]}$ , and the maximum error thereafter is only  $0.017 \text{ [rad]}$ .

In the estimation of  $\hat{\dot{\alpha}}$ , an initial inverse response is observed, with a maximum value of  $8.71 \times 10^{-2} \text{ [rad/s]}$ . However, after  $0.1 \text{ [s]}$ , the maximum error ( $e = \hat{\dot{\alpha}} - \dot{\alpha}$ ) never exceeds  $0.69 \text{ [rad/s]}$ , indicating good performances. (Before  $0.1 \text{ [s]}$ ,  $e_{max} = 2.11 \text{ [rad/s]}$  at  $0.023 \text{ [s]}$ ).

During the upcoming experiments, the comparison between measured positions and their estimated values will serve as the basis for evaluating the observer's performance.

### 4.3 Linear Quadratic Gaussian Regulator

LQG control is obtained by combining the LQ solution and a Kalman filter. The exigency of such an approach stems by the presence of stochastic noises spread into the process, formalizable as follows:

$$\begin{cases} \dot{x}(t) = Ax(t) + Bu(t) + v_x(t) \\ y(t) = Cx(t) + v_y(t) \end{cases} \quad (4.2)$$

where  $v_x$  models the uncertainty on the state knowledge, while  $v_y$  the uncertainty on the output measurement. For this system, the goal of LQG control is to minimize:

$$J = \lim_{T \rightarrow \infty} \frac{1}{T} E \left[ \int_0^T (x'(t) Q x(t) + u'(t) R u(t)) dt \right] \quad (4.3)$$

when the state  $x$  is nonmeasurable.

#### 4.3.1 LQ Infinity Control

The LQ infinity control law is found by minimizing with respect to  $u$  the following performance index:

$$J = \int_0^\infty (x'(t) Q x(t) + u'(t) R u(t)) dt \quad (4.4)$$

$Q$  and  $R$ , symmetric and positive semi-definite, are the weight matrices: the problem solution is optimal with respect to their choice.

The aim of this control strategy design is to achieve a robust controller in comparison to the controller obtained through Pole Placement in which we prioritized speed and responsiveness.

The choice of the two weights matrices is heuristic; it stems from a trial-and-error process, analogously as for eigenvalues assignment in Pole Placement design. The prescribed eigenvalues from the Pole Placement approach have been considered as reference in the design phase due to their good performances. In order to speed up the tuning process, the instrumental variable  $\alpha = 5$  was used to assign a prescribed rate of convergence to the closed loop poles. In doing so, the resulting poles always lay behind  $s = -\alpha = -5[\text{rad/s}]$  in the complex plane, regardless of  $Q$  and  $R$  choice.

#### State Weights $Q_{LQ} = C'_q C_q$

This is the weight of the state deviation from the origin during the transient.

By selecting a diagonal matrix for  $Q$ , we ensure the observability of the pair  $(A, C_q)$ . The elements on the main diagonal of  $Q$  correspond to the individual components of the state vector. Through their magnitudes, we introduced a penalty for deviations of the states from the equilibrium point. In our specific case, we assigned higher weights to the angular positions since our primary objective was to minimize the positional error and maintain  $\alpha = 0$ . Consequently, the weight associated with this variable was set to the highest value. We kept the weights on velocities relatively smaller as we aimed for a highly responsive controller.

To account for the differing magnitudes between angles and velocities around the equilibrium, a normalization term was included in the expression of the matrix  $Q$ . As a result, the weights used were as follows:

$$Q_{LQ} = \text{diag} \left( \frac{q_\theta}{\theta_{max,Q}^2}, \frac{q_\alpha}{\alpha_{max,Q}^2}, \frac{0.001}{5^2}, \frac{0.001}{5^2} \right) = \text{diag} \left( \frac{0.1}{\frac{\pi^2}{2}}, \frac{1}{0.44^2}, \frac{0.001}{5^2}, \frac{0.001}{5^2} \right) \quad (4.5)$$

#### Input Weights $R_{LQ}$

The weight matrix  $R$  is used to penalize the control action, providing better control over the saturation constraints imposed by the actuator.

Although choosing a larger value for  $R$  compared to  $Q$  may slow down the speed of the closed-loop system, it enhances its robustness. Similarly to the weight matrix  $Q$ , a normalizing term was introduced in the expression of the matrix  $R$  for the same reasons mentioned earlier.

$$R_{LQ} = \frac{r_V}{v_{max,R}^2} = \frac{50}{10^2} \quad (4.6)$$

## Results

The resulting gain matrix is:

$$K_{LQ,\alpha} = [-20.66, 66.53, -7.84, 9.77] \quad (4.7)$$

and the associated closed loop poles are:  $\{-17 + i3.2, -17 - i3.2, -10.05, -7.93\}$ . The specifications on  $\alpha$ , the only state variable with non-zero initial state, are the same used for the Pole Placement, and reported at the beginning of the chapter. The simulation results are the following:

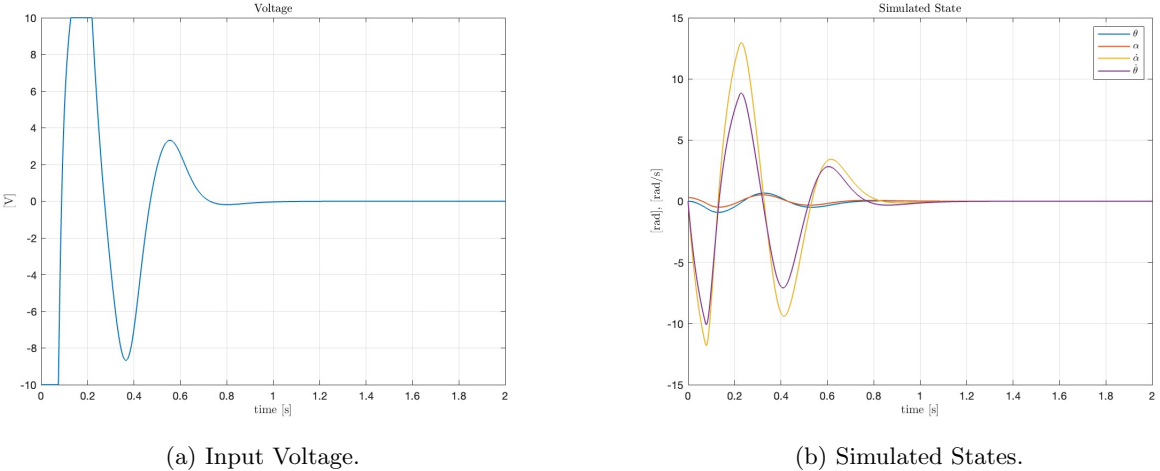


Figure 4.4: LQ Controller in Simulation.

This simulation was performed with the worst initial condition for  $\alpha$  ( $0.3[\text{rad}]$ ) that the controller can stabilize. Even under such a condition, the design specifications are satisfied, specifically:

$\theta_{t_s=1.5}$	$\alpha_{t_s=1.5}$	$\dot{\theta}_{t_s=1.5}$	$\dot{\alpha}_{t_s=1.5}$	$\Delta t_{10}[\text{V}]$	$t_s$	$e_\infty$
$3.97 \times 10^{-5}$	$-5.43 \times 10^{-5}$	$2 \times 10^{-5}$	$-5.5 \times 10^{-4}$	0.09 [s]	0.82 [s]	0

Table 4.2: Simulation Data.

The table demonstrates the superior stabilization capability of the LQ controller compared to the Pole Placement solution. Despite initiating from higher values of  $\alpha$  ( $\alpha_{lq} = 0.3[\text{rad}] > \alpha_{pp} = 0.13[\text{rad}]$ ), the LQ controller still achieves stabilization. Notably, the LQ controller also exhibits improved speed, evident by the settling time of  $t_s = 0.96[\text{s}]$  for an initial  $\alpha$  value of  $0.13[\text{rad}]$ , compared to the Pole Placement's settling time of  $1.3[\text{s}]$ .

### 4.3.2 Kalman Filter

In order to implement the LQ control law on the physical setup, a Kalman Filter was developed to estimate the angular speeds,  $\dot{\theta}$  and  $\dot{\alpha}$ . The Kalman Filter is an optimal estimator designed for systems affected by additive stochastic disturbances represented as white Gaussian noises. In this implementation, we made a simplifying assumption by neglecting any cross-correlation between the input and output, even though the output equation is given by  $y = C x$ .

The tuning of the Kalman Filter primarily took place in the laboratory setting. This decision was made because the imaginary component of the estimator's poles exhibited less controllability and higher magnitudes compared to the Pole Placement counterpart. Consequently, these characteristics led to undesired oscillatory behavior of the horizontal arm around the equilibrium.

Throughout the tuning process, the behavior of  $\alpha$  and  $\hat{\alpha}$  (estimated angular velocities) were utilized as reference metrics. This choice was motivated by the same reasons mentioned in the Pole Placement design chapter.

$$Q_{KF} = C'_{qKF} C_{qKF}$$

This weight, a  $4 \times 4$  matrix, models the confidence on the corresponding state components through the associated elements in its diagonal. In fact, the diagonal entries of this matrix are associated to the variances of the uncertainties on the state components value. The designed matrix is:

$$Q_{KF} = \text{diag}(9, 8, 7.5 \times 10^3, 3.7 \times 10^3) \quad (4.8)$$

We assigned smaller weights to angular positions compared to angular speeds due to the higher variances associated with the latter. By doing so, the algorithm was compelled to update the velocity estimates more frequently than the position estimates.

As a final observation, the weight on  $\theta$  was set to be greater than the weight on  $\alpha$  because the identified model demonstrated poorer performance in accurately describing the angular position  $\theta$  in comparison to  $\alpha$ .

$$R_{KF}$$

This weight models our confidence in the measurements. By a probabilistic point of view, its entry is associated to the variance of the noise acting on the output measures. Being our sensors pretty accurate, we tended to set low values in this matrix. Moreover, a large  $\frac{Q}{R}$  ratio speeds up the estimate convergence.

$$R_{KF} = \text{diag}(3 \times 10^{-3}, 1.5 \times 10^{-3}) \quad (4.9)$$

## Results

The Kalman filter gain matrix is

$$L_{KF} = \begin{pmatrix} 66.2 & -6.73 \\ -3.4 & 95.01 \\ 702.4 & -323.9 \\ -380.9 & 1858.5 \end{pmatrix} \quad (4.10)$$

The associated closed loop poles are:  $\{-36.72+i8.39, -36.72-i8.39, -34.28, -70.53\}$ . The specifications for the Kalman Filter were set to be the same as the ones for the Luenberger Observer.

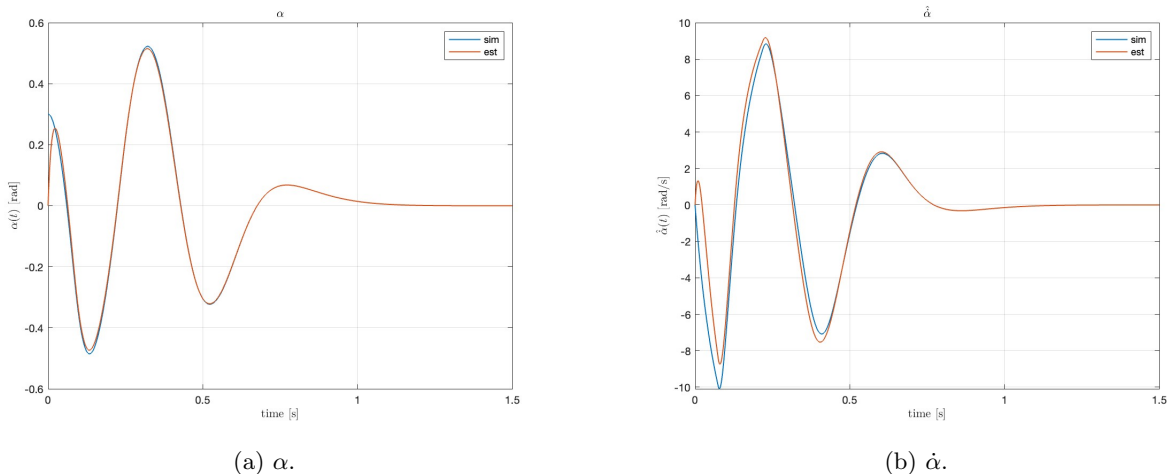


Figure 4.5: Kalman Filter Simulation and Estimation.

The figure demonstrates the Kalman filter's performance in estimating  $\hat{\alpha}$  and  $\hat{\dot{\alpha}}$ .

The initial error, resulting from the difference between the worst initial condition for  $\alpha$  and zero initial condition for the observer, is 0.3 [rad]. The estimated  $\hat{\alpha}$  intersects with the simulated line at 0.02 [s], and the maximum error thereafter is only 0.034 [rad].

In the estimation of  $\hat{\alpha}$ , an initial inverse response is observed, with a maximum value of 1.33 [rad/s]. However, after 0.1[s], the maximum error ( $e = \hat{\alpha} - \dot{\alpha}$ ) never exceeds 0.013[rad/s], indicating favorable performance. (Before 0.1[s],  $e_{max} = 4.27$  [rad/s] at 0.023[s]).

## 4.4 Tracking of $\theta$

After successfully attaining satisfactory performance with the stabilizing controllers, our attention turned towards the design of tracking controllers. The state has been enlarged as follows:

$$\tilde{x} = \begin{pmatrix} \theta \\ \alpha \\ \dot{\theta} \\ \dot{\alpha} \\ \eta \end{pmatrix}, \dot{\eta} = y - y^{ref} \quad (4.11)$$

where  $\eta$  accounts for the dynamics of an integrator.

Simulations have been performed using a square input signal characterized by an amplitude of 0.3 [rad] and a frequency of 0.1 [Hz]. In this analysis, we imposed a minimum settling time requirement on the controller while also considering voltage saturation limits.

### 4.4.1 Pole Placement

To achieve successful tracking, it was necessary to add an integrator to the system. Before doing so, we performed a preliminary check to ensure that the system had no invariant zeros at the origin. Once this condition was verified, we proceeded to examine the transfer function  $G_{V\theta}$  to confirm that it did not have any derivative action ( $s \neq 0$ ). Additionally, we checked that the number of outputs  $p$  was less than or equal to the number of inputs  $m$ .

$$G_{V\theta}(s) = \frac{27.22(s + 6.75)(s - 6.29)}{s(s + 17.02)(s + 6.42)(s - 6.41)}$$

### System Enlargement

To enlarge the system, we compute the state space matrices using the following commands:

$$\tilde{A} = [A \text{ zeros}(n,pc); -C(1,:) \text{ zeros}(pc)]; \quad \tilde{B} = [B; \text{zeros}(pc)];$$

where  $n = 4$  represents the system order,  $pc = 1$  is the number of controllable inputs, and  $A$ ,  $B$ ,  $C$ , and  $D$  are the matrices of eq.1.25.  $\tilde{A}$  is a  $5 \times 5$  matrix, and  $\tilde{B}$  is a  $5 \times 1$  matrix.

### Pole Placement Controller Design for the Enlarged System

The desired specifications, with  $\theta$  as the control variable, are as follows: zero steady-state error ( $e_\infty = 0$ ), settling time ( $t_s$ ) less than or equal to 1.5 [s], overshoot within 5%, and a maximum voltage saturation time of 0.1[s]. We do not set any constraints on the initial inverse response of  $\theta$ .

Following the approach described in Section 4.1, we place the poles position for the enlarged system in:  $\{-4.9 - 7i, -4.9 + 7i, -5, -5, -15\}$ . The fifth pole is set empirically to a lower value until specifications are satisfied.

The resulting controller gains are found through the command:

$$K_{en} = \text{place}(\tilde{A}, \tilde{B}, [-4.9 - 7i, -4.9 + 7i, -5, -5, -15]).$$

Finally, we split the gain as  $K_{en} = [K_{en,x}, K_{en,\eta}] = [-14.51, 38.84, -4.71, 5.75, 23.72]$ . Where the last value represents the gain associated to the integrator dynamics ( $K_{en,\eta}$ ).  
The simulation results with this controller are presented below:

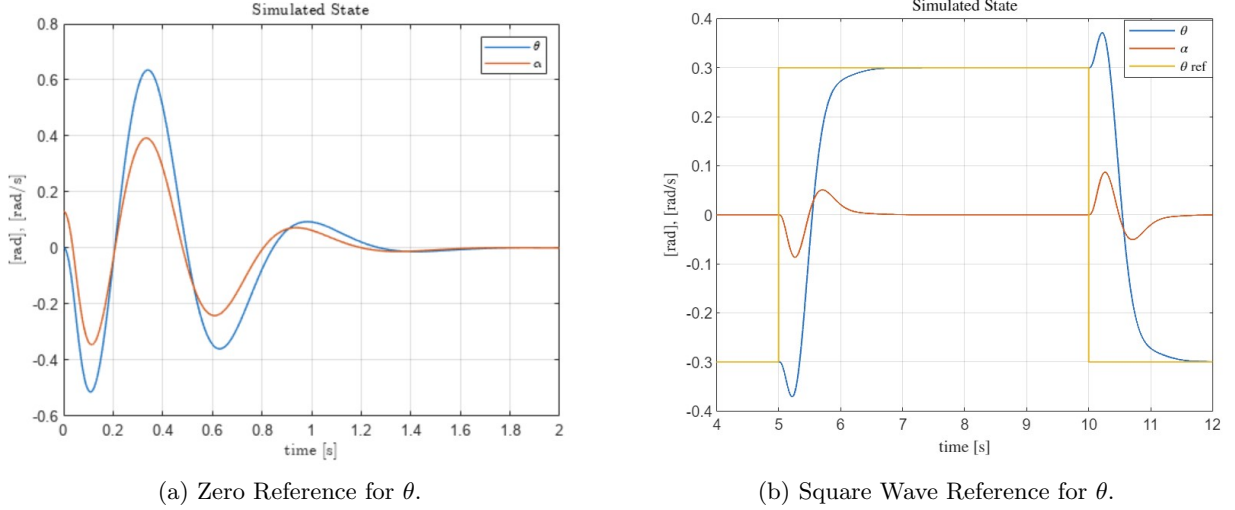


Figure 4.6: Different Reference for  $\theta$  with Pole Placement Tracking Controller.

	Overshoot %	Inverse resp. [rad]	Max. voltage [V]	$\Delta t_{10V}[s]$	$t_s[s]$	$e_\infty$	$t_r[s]$
P.p zero ref	/	/	10	0.029	1.11	0	/
P.p square ref	0 %	0.07	1.03	/	1.25	0	0.445

Table 4.3: Simulation Data.

Giving a zero reference value for  $\theta$ , allow to assess the stabilization capabilities of the controller and the settling time ( $t_s$ ) is computed with respect to the behaviour of  $\alpha$ . Note that the initial displacement of  $\alpha$  is 0.13 [rad]. For this scenario specifications the same as in Section 4.1.

When the reference is different from zero, we are more interested in the evolution of  $\theta$ . From Table 4.3 we can see how the specifications formulated at the beginning of this chapter are successfully met.  
As a side note, we performed the estimation of the non measurable state components with the same observer introduced in Section 4.2.

#### 4.4.2 LQG Control

The specifications on  $\theta$  are the same used in the tracking with the Pole Placement a part from the settling time that is set to be lower than 2 [s].

Being the state enlarged, the weight matrix  $Q$  was correspondingly updated, by adding a fifth element in its diagonal. Such an element penalizes state of the integrator. The larger this weight, the smaller the settling time of the tracking, at the cost of higher input voltages.

Also here, a prescribed rate of convergence was assigned to the closed loop, having set the auxiliary variable  $\alpha = 2$ .

$$\tilde{Q}_{LQ} = \text{diag}(1 \times 10^{-3}, 1, 1 \times 10^{-3}, 1 \times 10^{-3}, 1 \times 10^{-4}) \quad (4.12)$$

It is worth noting that the weight assigned to  $\theta$  is ten times greater than the weight applied to penalize dynamic error deviation. This deliberate choice was made to prioritize the effectiveness of stabilizing the angular position rather than achieving precise tracking of the reference signal. As a result, the resulting control law demonstrated enhanced robustness compared to the Pole Placement controller.  
Finally, the input weight has been set to:

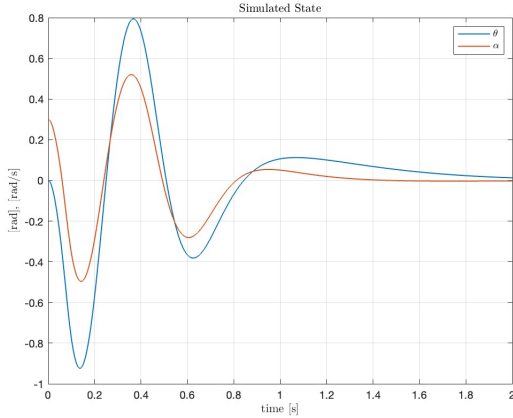
$$\tilde{R}_{LQ} = 0.10 \quad (4.13)$$

## Results

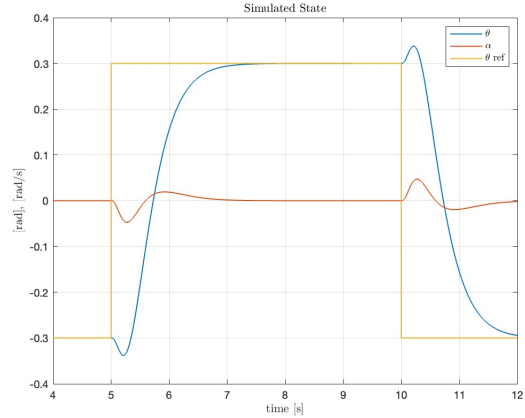
The resulting gain matrix is:

$$\tilde{K}_{LQ,\alpha} = [10.33, -3.91, 1.82, 1.27, -14.53] \quad (4.14)$$

and the associated closed loop poles are:  $\{-5.24+i6.21, -5.24-i6.21, -4+i0.014, -4-i0.014, -15.86\}$ . With this controller, the resulting simulations are the following:



(a) Zero reference for  $\theta$ .



(b) Square Wave Reference for  $\theta$ .

Figure 4.7: Different Reference for  $\theta$  with LQG Tracking Controller.

	Overshoot %	Inverse resp. [rad]	Max. voltage [V]	$\Delta t_{10V}[s]$	$t_s [s]$	$e_\infty$	$t_r [s]$
LQG zero ref	/	/	10	0.07	1.34	0	/
LQG square ref	0 %	0.04	0.54	/	1.79	0	0.864

Table 4.4: Simulation Data.

Giving a zero reference value for  $\theta$ , allow to assess the stabilization capabilities of the controller and the settling time ( $t_s$ ) is computed with respect to the behaviour of  $\alpha$ . Note that the initial displacement of  $\alpha$  is 0.3 [rad]. For this scenario specifications the same as in Section 4.1.

When the reference is different from zero, we are more interested in the evolution of  $\theta$ . From Table 4.4 we can see how the specifications formulated at the beginning of this chapter are successfully met.

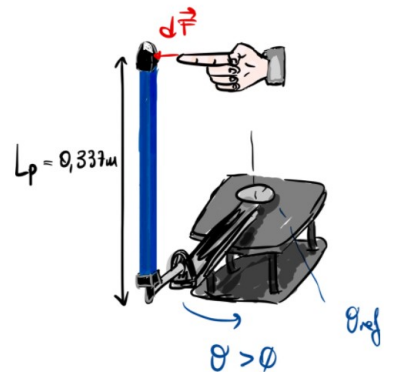
As a side note, we performed the estimation of the non measurable state components with the Kalman Filter introduced in Section 4.3.2.

### 4.4.3 Robustness of Tracking

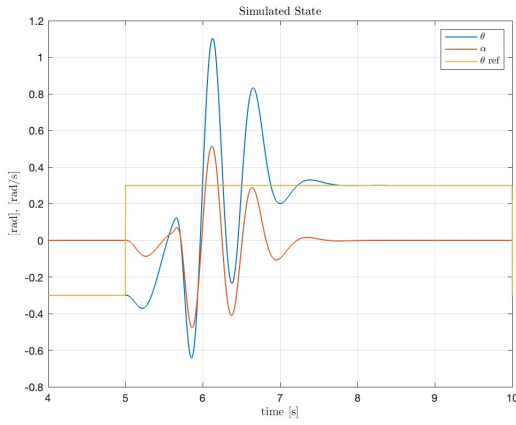
The robustness of the tracking controllers has been assessed first in simulation and then in the laboratory.

To this aim, the dynamic model of the system has been rewritten considering an external force acting on the tip of the pendulum. In the worst conditions, this force would produce a moment  $M_d = \pm L_p \delta F$ .

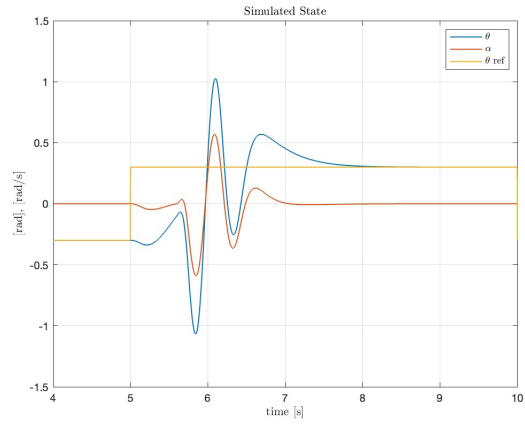
In our simulations, we assumed positive values for  $M_d$ , produced by an impulsive excitation acting for 0.1 [s] while  $\theta$  was moving in the positive direction. In this way, the disturbance would cause the pendulum to move in the opposite direction with respect to the tracked trajectory. We then iteratively searched for the maximum value of the force  $F$  that could be applied while the controller was still managing to accomplish the tracking.



We test the robustness in the simulation, obtaining the following results:



(a) Pole Placement.



(b) Linear Quadratic Gaussian.

Figure 4.8: Robustness of Tracking Controllers Under Impulsive Disturbances in Simulation.

For the Pole Placement controller an impulsive force of  $F = 0.05[N]$  was the maximum applicable and the maximum voltage reached during the stabilization maneuver is  $7.88[V]$ .

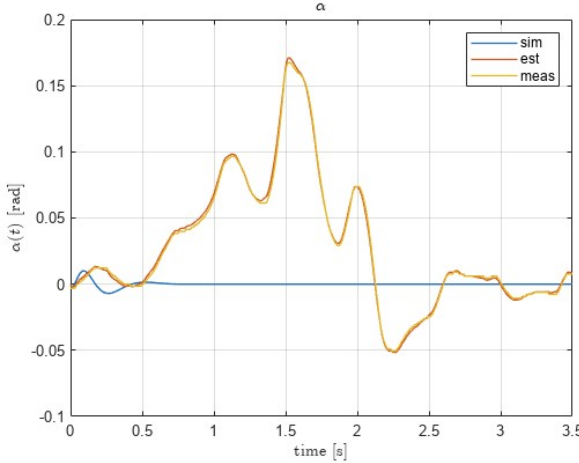
For the LQG regulator, a force  $F = 0.075[N]$  was the highest possible and the voltage saturates for just  $0.05[s]$ .

## 4.5 Experiments

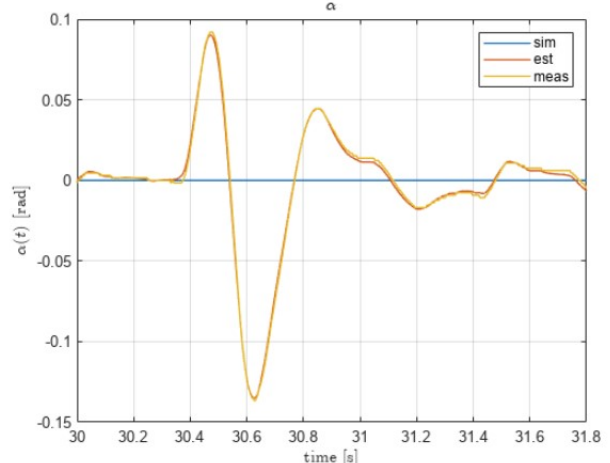
This section presents significant experiments conducted for each controller using different velocity estimation strategies. A summary table highlighting the main characteristics of each experiment will be provided at the end of the chapter.

Throughout all the tracking experiments, a square wave signal with an amplitude of  $3 [rad]$  and a frequency of  $0.1 [Hz]$  was utilized.

### 4.5.1 Pole Placement Experiments

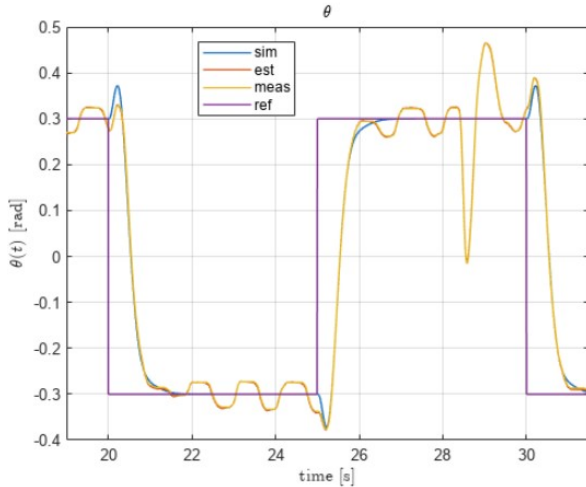


(a) Initial Conditions of  $\alpha$ .

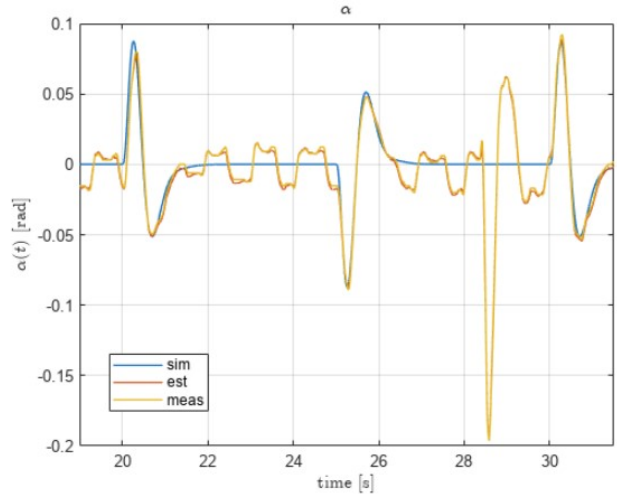


(b) Disturbance Acting on  $\alpha$ .

Figure 4.9: Pole Placement Experiment for the Stabilization of  $\alpha$  with Observer.



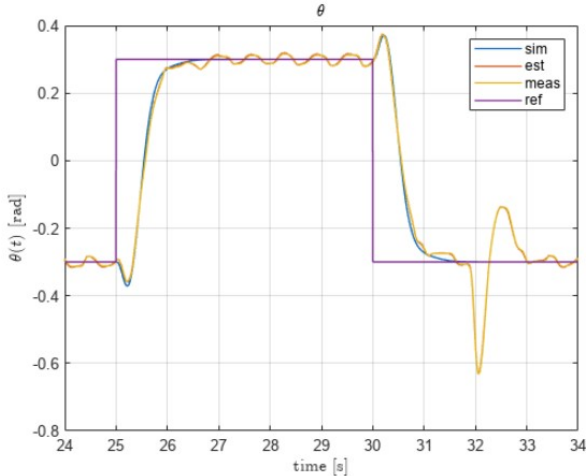
(a) Tracking of  $\theta$ .



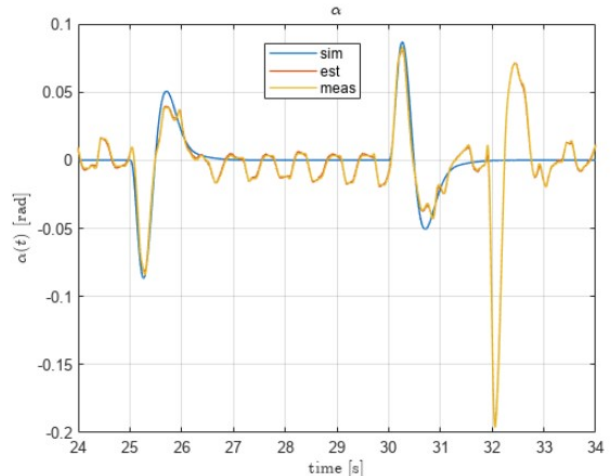
(b) Performances of  $\alpha$ .

Figure 4.10: Pole Placement Experiment for the Tracking of  $\theta$  with Observer.

The employed controller in these tracking experiments demonstrated a fast response; however, it exhibited limited robustness against disturbances, particularly during the transient phase. If a more robust controller is desired, it is advisable to prioritize stabilization over precise tracking. Notably, at time  $t = 28$  [s], the controller successfully stabilizes the system even in the presence of a small disturbance, as depicted in Figure 4.10.



(a) Tracking of  $\theta$ .



(b) Performances of  $\alpha$ .

Figure 4.11: Pole Placement Experiment for the Tracking of  $\theta$  with Kalman Filter.

#### 4.5.2 LQG Experiments

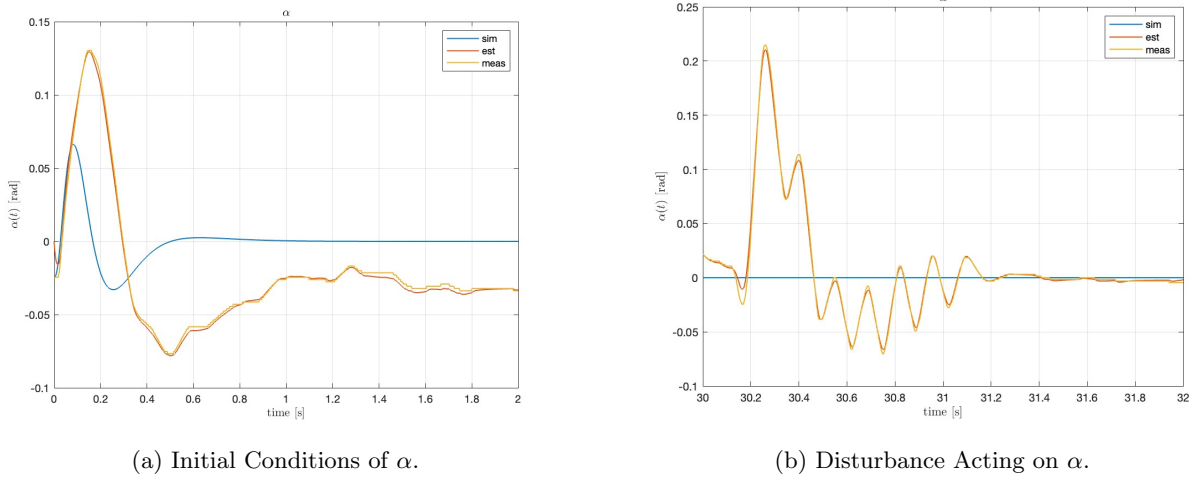


Figure 4.12: LQG Experiment for the Stabilization of  $\alpha$  with Luenberger Observer.

In Figure 4.12a, a slight offset can be observed in the stabilization, deviating from the zero position. This offset may be attributed to the manual adjustment of the reference zero position before starting the experiment, which might not have been sufficiently close to the absolute zero, or to a potential error in the encoder measurement. However, it is important to note that despite this offset, the performance of the controller is not affected, and it effectively stabilizes the pendulum.

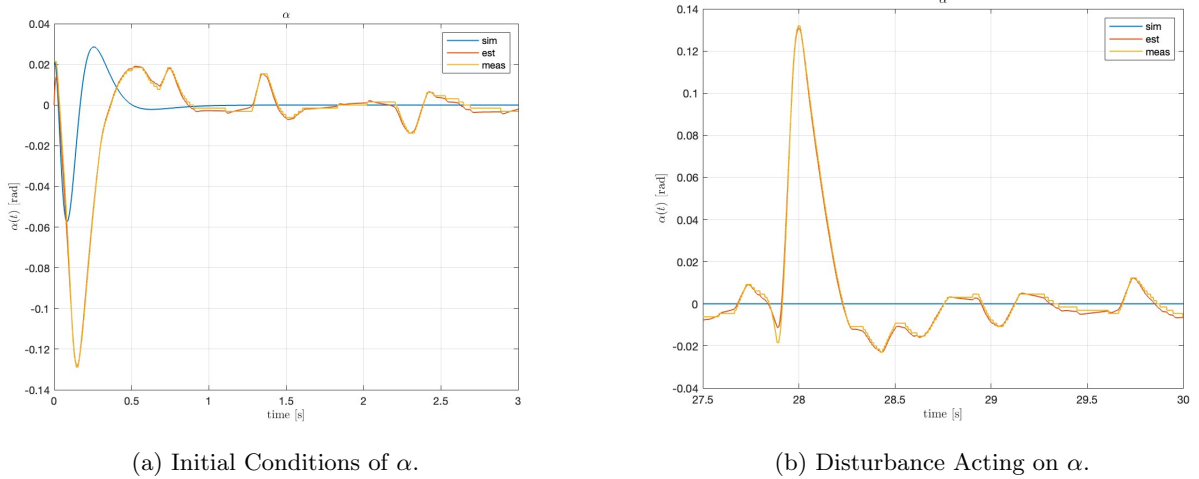


Figure 4.13: LQG Experiment for the Stabilization of  $\alpha$  with Kalman Filter.

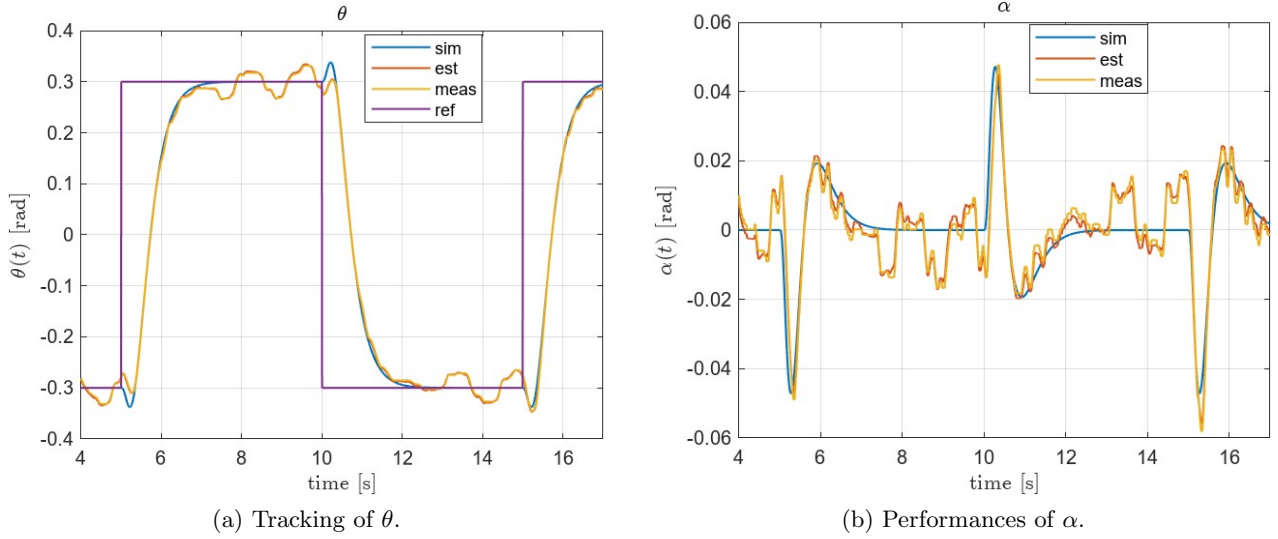


Figure 4.14: LQG Experiment for the Tracking of  $\theta$  with Luenberger Observer.

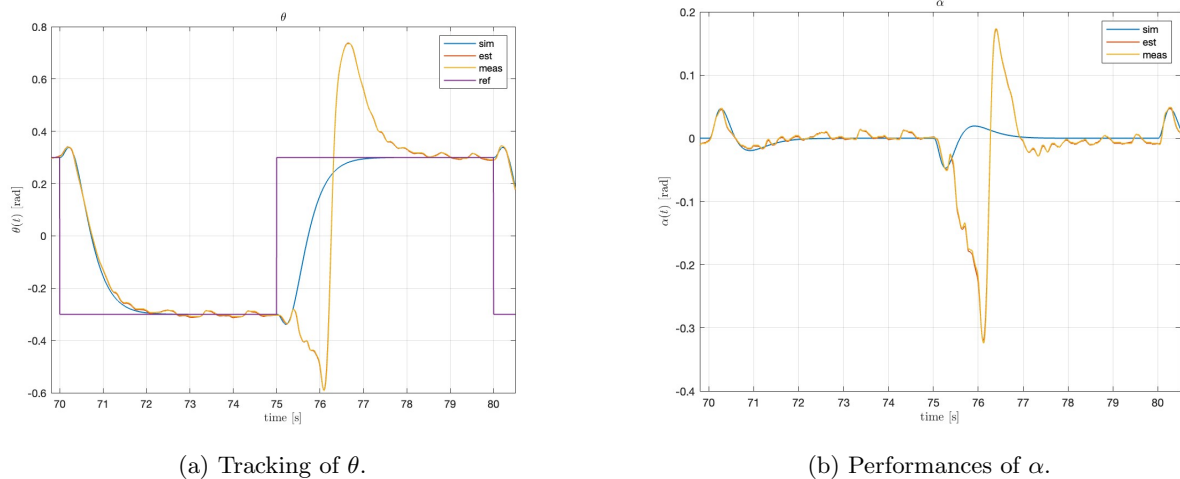


Figure 4.15: LQG Experiment for the Tracking of  $\theta$  with Kalman Filter.

The controller in these tracking experiments demonstrated a slower response with respect to the Pole Placement; however, it exhibited higher robustness against disturbances. This has been possible by the choice of the weights of the matrix  $Q$ .

#### 4.5.3 Comparison and Final Notes

	Max. voltage nom. / dist.	$t_d$	$t_r$	$e_\infty$	Robust	Inverse response
P.p. stab. obs.	0.5 / 6 [V]	0.73 [s]	/	$\pm 8 \times 10^{-3}$ [rad]	Medium	/
LQG stab. obs.	4.91/7.6 [V]	1.02 [s]	/	$\pm 6 \times 10^{-3}$ [rad]	High	/
LQG stab. Kf	3.89/7.2 [V]	0.87 [s]	/	$\pm 14 \times 10^{-3}$ [rad]	High	/
P.p. track. obs.	1.5 / 6.1 [V]	1.13 [s]	0.42 [s]	$\pm 0.03$ [rad]	Low	0.09 [rad]
P.p. track. Kf	1.44 / 6.1 [V]	1.11 [s]	0.53 [s]	$\pm 0.026$ [rad]	Low	0.07 [rad]
LQG track. obs.	1.02/5.69 [V]	2.36 [s]	0.94 [s]	$\pm 0.07$ [rad]	Very high	0.05 [rad]
LQG track. Kf	1.05/7.61 [V]	1.99 [s]	1.02 [s]	$\pm 0.016$ [rad]	Very high	0.04 [rad]

Table 4.5: Experimental Data.

Table 4.5 provides data summarizing the different experiments. For the experiments evaluating stabilizing controllers it displays:

- Maximum voltage applied to the system at the beginning of the experiment, and while a small disturbance was acting on the system as modeled in Section 4.4.3.
- $t_d$ , the time required to stabilize the system after perturbing  $\alpha$ , and it is computed from the figures above.
- $e_\infty$ , which represents the error of the controller at steady state.
- A qualitative index of robustness of the controller.

Regarding the values of  $t_d$ , we observe that they are lower than the corresponding settling times computed in simulation. This difference can be attributed to the less critical conditions experienced in the laboratory compared to the simulated scenario (Table 4.1, Table 4.2). At steady state, it is evident that the LQ regulator with the Kalman Filter (KF) performs the worst among the controllers. This could be attributed to the sub-optimal noise rejection capabilities of the KF, as its pole locations have higher imaginary parts compared to the Pole Placement controller. As expected, the LQ solution demonstrates better robustness.

Turning our attention to the tracking experiments:

- Maximum voltage applied to the system while following the reference, and while this task was afflicted by a disturbance (Table 4.1)
- $t_d$ , the time needed by the controller to reach the steady state error region
- $t_r$ , the rise time, computed as in Table 5.7
- $e_\infty$ , which represents the error of the controller at steady state
- A qualitative index of robustness of the controller
- The maximum displacement associated to the initial inverse response

The conducted experiments closely aligned with our design choices, confirming the effectiveness of our approach. The implementation of the Pole Placement controller yielded a faster and more responsive solution. However, it exhibits reduced robustness compared to the LQG control law.

Additionally, it is worth noting that the LQG controller exhibits a significantly lower steady-state error when using the Kalman filter compared to the Luenberger observer. This difference can be attributed to the faster dynamics of the optimal filter, which may allow some noise to pass through the filtering process. As a result, oscillations with smaller amplitudes but higher frequencies may be observed. On the other hand, the Pole Placement method permits wider oscillations with lower frequencies, providing a different response characteristic.

## 5. Swing Up Control

The objective of the swing-up maneuver is to transition the pendulum position from a stable equilibrium to an unstable one.

Once the unstable equilibrium is reached, a stabilizing controller must be activated to balance the system and maintain it around the upright position.

In our work, we primarily referred to the approach presented in [1]. However, we made some additional modifications during the design phase to meet specific constraints on the state evolution.

The following sections provide a brief explanation of the Partial Feedback Linearization (P.F.L.) procedure, followed by the design of the energy controller. We also touch upon the stabilizing controller and introduce the design of an Extended Kalman Filter. Finally, we compare simulation and experimental results, while also conducting an empirical analysis of the repeatability of the control law.

### 5.1 Partial Feedback Linearization: P.F.L.

The main goal behind P.F.L. is to rewrite the model of the rotary inverted pendulum in a simplified form. We want to bring ourselves back to the model of a simple inverted pendulum, hinged at one of its ends and free to swing around this single degree of freedom. The linearization can be only partial because the system is under-actuated, and we performed it with respect to the actuated variable, which in our case is  $\theta$ , obtaining what is known as "collocated linearization".

We refer to [1] for the general P.F.L. procedure for a generic under-actuated dynamical system.

By appropriately designing the torque  $\tau$  as a function of the desired angular acceleration  $u$ , we get the following dynamics:

$$\begin{cases} \ddot{\theta} = u \\ \ddot{\alpha} = \frac{l_p m_p r \cos(\alpha)}{J'_p} u + \frac{m_p \cos(\alpha) \sin(\alpha) l_p^2 \dot{\theta}^2 + g m_p l_p \sin(\alpha)}{J'_p} \end{cases} \quad (5.1)$$

Here,  $J'_p = m_p l_p^2 + J_p$  represents the moment of inertia of the pendulum about its pivot.

And in state space form we have:

$$\begin{cases} \dot{x}_1 = x_3 \\ \dot{x}_2 = x_4 \\ \dot{x}_3 = u \\ \dot{x}_4 = \frac{l_p m_p r \cos(x_2)}{J'_p} u + \frac{m_p \cos(x_2) \sin(x_2) l_p^2 x_3^2 + g m_p l_p \sin(x_2)}{J'_p} \end{cases} \quad (5.2)$$

In this representation, the angular acceleration of the pendulum depends on a input  $u$ , a gravitational term, and a term related to centrifugal acceleration (proportional to  $x_3^2$ ).

The goal now is to drive the state variables to  $\mathbf{x}^0 = (\bar{x}_1, 0, 0, 0)^T$ , following the conventions shown in Fig.1.1. With  $\bar{x}_1$  being any angle in the range  $\pm \frac{\pi}{3}$  [rad].

### 5.2 Energy Control

Once we have the partially linearized model, we can proceed with the design of an energy-based controller for the swing-up maneuver. To this aim, the potential energy of the system is redefined such that it is maximum in the upright position:

$$V = g m_p l_p (1 + \cos(x_2)) \quad (5.3)$$

The objective of the controller is to reduce the error  $\tilde{E}(t) = E_p(t) - E_d$  to zero, where  $E_p(t)$  represents the total energy of the pendulum at a given time instant, and  $E_d$  is the energy associated with the upright position, namely  $E_d = 2 g m_p l_p = 0.073[J]$ .

The convergence of  $\tilde{E}$  to zero is achieved by the following control law, as it can be shown in [1]:

$$u = -400 x_4 \cos(x_2) \tilde{E} - \frac{l_p}{r} x_3^2 \sin(x_2) \quad (5.4)$$

In this control law, the term  $\frac{l_p}{r} x_3^2 \sin(x_2)$  compensates for the centrifugal effect caused by the rotation of the base.

Despite achieving successfully the swing up maneuver, while satisfying the usual limits imposed on saturation of the input voltage, this control law would not allow to restrict the values of  $\theta$  within  $\pm \frac{\pi}{3}$  [rad]. To address this, a proportional-derivative (PD) controller is added, as reported in [2].

The gains of the proportional and derivative actions,  $K_p$  and  $K_d$  respectively, are tuned in simulation to restrict  $\theta$  within the specified range. For our system, the values  $K_p = 100$  and  $K_d = 2$  were found to be effective.

The complete control law is then given by:

$$u = -400 x_4 \cos(x_2) \tilde{E} - \frac{l_p}{r} x_3^2 \sin(x_2) - 100 x_1 - 2 x_3 \quad (5.5)$$

It is noteworthy that the inclusion of the PD controller also contributed to achieving a quicker completion of the swing-up maneuver.

Moreover, our system necessitates a voltage input rather than an acceleration signal. As a result, the desired acceleration  $u$  is converted into the corresponding torque value  $\tau(u)$ , which is subsequently transformed into the applied voltage  $V_m$  using the relationship specified in Eq. 1.15.

### 5.2.1 Stabilizing Controller and Switching Logic

When the absolute value of  $\alpha$  is less than or equal to 0.3 [rad], the tracking-oriented LQ controller (Eq. 4.14) is activated and remains active as long as  $\alpha$  remains within  $\pm 0.5$  rad. To simplify the problem, the value  $\bar{x}_1 = \bar{\theta}$  at the time of LQ controller activation is recorded and utilized as the reference position for the horizontal arm. This approach simplifies the stabilization of  $\alpha$  and reduces the actuator's effort requirement.

Furthermore, the tracking capabilities of the stabilizing controller are employed to bring the horizontal arm to an absolute  $\theta = 0$  position, which corresponds to the initial configuration prior to the swing-up maneuver. This allows for the execution of subsequent experiments, all starting from the same initial configuration.

### 5.2.2 The Extended Kalman Filter

Both the stabilizing and energy-based controllers relied on measured values from encoders and from the estimation of the speeds provided by an Extended Kalman Filter (EKF). The utilization of this non-linear estimator was necessary due to the high non linearity of the trajectories of the system. As the EKF is a well-established estimator, we omit the detailed implementation. The algorithm we referred to can be found in [4].

The tuning of the covariance matrices followed the same assumptions as described in Section 4.3.2. Thus, the process and measurement variances were kept equal, and their specific values can be found in the previous sections. Both simulation and real experiments demonstrated satisfactory estimation performance.

## 5.3 Validation of the Control Law

### 5.3.1 Dealing with Initial Conditions

During the implementation of the control law on the physical hardware, it was observed that the performance of the energy controller was significantly affected by the initial conditions. This lack of repeatability led to unpredictable behavior of the system.

To mitigate this issue, a small impulsive voltage of 0.1 [V] with a duration of 0.01 [s] was applied as an initial step.

The complete control law utilized in both the experimental and simulation setups is as follows:

$$V_m = \begin{cases} 0.1 & \text{if } t \leq 0.01[\text{s}] \\ a_1\tau(u_{energy}) + a_2\hat{x}_3 & \text{if } t > 0.01[\text{s}] \\ -K_{lq}(\mathbf{x}^0 - \mathbf{x}) & \text{if } t > 0.01[\text{s}], |x_2| < 0.3 [\text{rad}] \end{cases} \quad (5.6)$$

Here,  $a_1 = \frac{R_m}{\eta_g \eta_m K_g k_t}$ ,  $a_2 = K_g k_m$ , and  $\hat{x}_3$  represents the estimated value of  $\dot{\theta}$  obtained from the EKF.  $\mathbf{x}^0 = (\bar{x}_1, 0, 0, 0)^T$  represents the equilibrium configuration at the switching moment.

### 5.3.2 Simulation and Experimental Results

In the real setup, it was observed that the swing-up process occurred faster compared to the results obtained from the simulation. This disparity could be attributed to several factors, such as unaccounted friction effects that affect the movement of the horizontal arm in the physical system. However, despite this discrepancy in timing, it is evident that the general pattern of the swing-up process is consistent and well-matched between the experimental and simulated outcomes.

#### Voltage

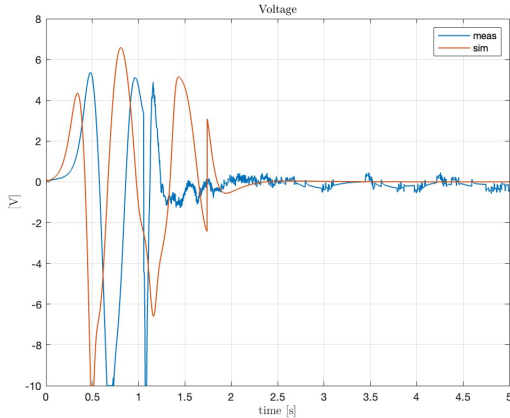


Figure 5.1: Input Voltage.

	$V_{max}$ [V]	$V_{min}$ [V]	$\Delta t_{10[V]}$ [s]
Sim.	6.58	-10	0.032
Exp.	5.37	-10	0.06

Table 5.1: Swing Up Saturation Specifications.

Both in simulation and experimental settings, the specification in terms of saturation is met and satisfied.

#### Theta

	$\theta_{max}$ [rad]	$\theta_{min}$ [rad]	$\theta_{ref}$ [rad]	$\dot{\theta}_{max}$ [rad/s]	$\dot{\theta}_{min}$ [rad/s]
Simulation	0.99	-0.95	0.51	8.83	-11.23
Experimental	1.06	-1.01	-0.65	6.60	-13.19

Table 5.2: Significant Values of  $\theta$  and  $\dot{\theta}$  during Swing Up.

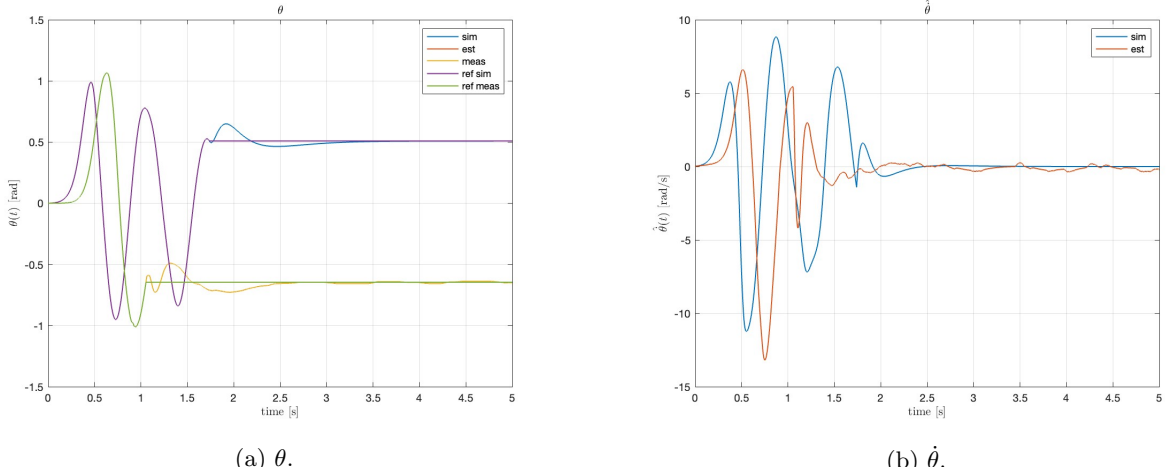


Figure 5.2:  $\theta, \dot{\theta}$  Simulated and Experimental.

Alpha

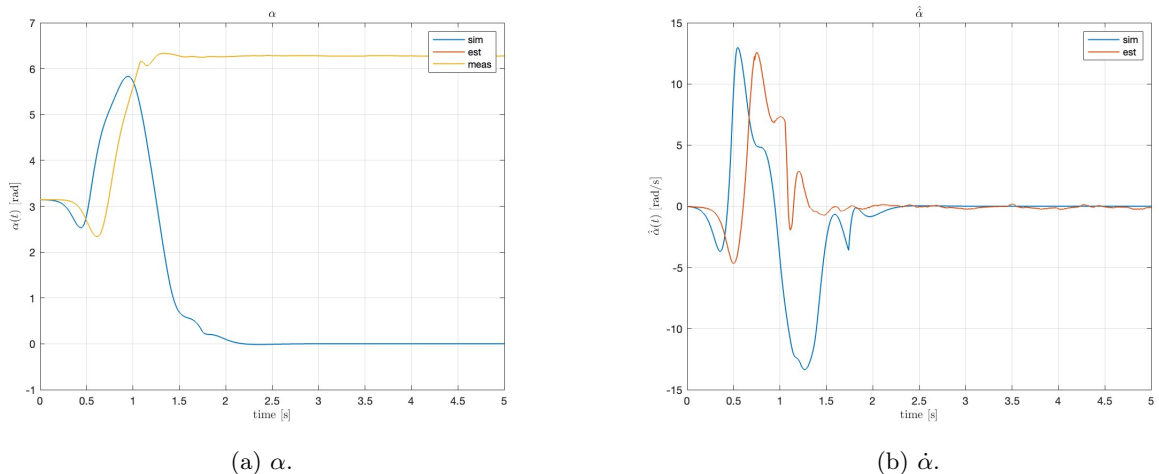


Figure 5.3:  $\alpha, \dot{\alpha}$  Simulated and Experimental.

	$\alpha_{min} [rad]$	$t_{switch} [s]$	$\dot{\alpha}_{max} [rad/s]$	$\dot{\alpha}_{min} [rad/s]$
Simulation	2.53	1.74	12.98	-13.36
Experimental	2.34	1.05	12.59	-4.69

Table 5.3: Significant Values of  $\alpha$  and  $\dot{\alpha}$  during Swing Up.

### 5.3.3 Repeatability

From the figures below, we can observe that different experiments yielded very similar behavior of the state variables and the control input.

## Voltage

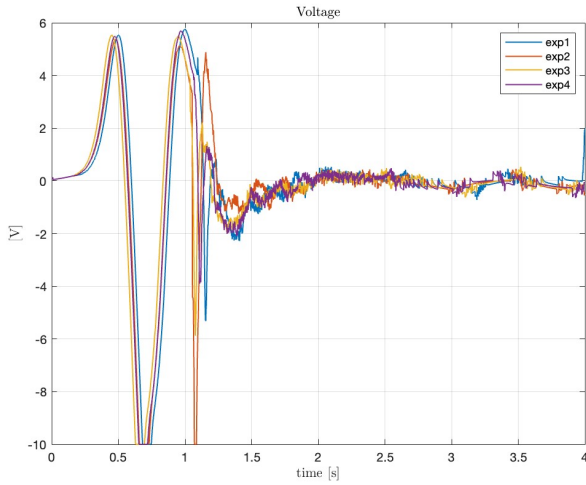
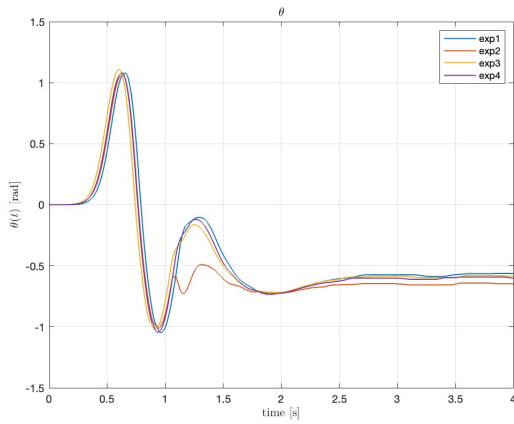


Figure 5.4: Input Voltage.

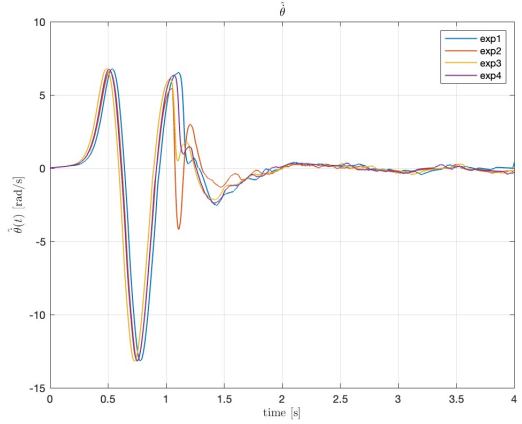
	$V_{\max} [V]$	$V_{\min} [V]$	$\Delta t_{10[V]} [s]$
Exp.1	5.52	-10	0.064
Exp.2	5.37	-10	0.06
Exp.3	5.76	-10	0.064
Exp.4	5.69	-10	0.064

Table 5.4: Swing Up Saturation Specifications.

## Theta



(a)  $\theta$ .



(b)  $\dot{\theta}$ .

Figure 5.5:  $\theta, \dot{\theta}$  Experimental.

	$\theta_{\max} [\text{rad}]$	$\theta_{\min} [\text{rad}]$	$\theta_{ref} [\text{rad}]$	$\dot{\theta}_{\max} [\text{rad/s}]$	$\dot{\theta}_{\min} [\text{rad/s}]$
Exp.1	0.1.08	-1.05	-0.57	6.78	-13.15
Exp.2	1.06	-1.01	-0.65	6.60	-13.19
Exp.3	1.11	-1.02	-0.58	6.79	-13.18
Exp.4	1.08	-1.04	-0.60	6.75	-13.14

Table 5.5: Significant Values of  $\theta$  and  $\dot{\theta}$  during Swing Up.

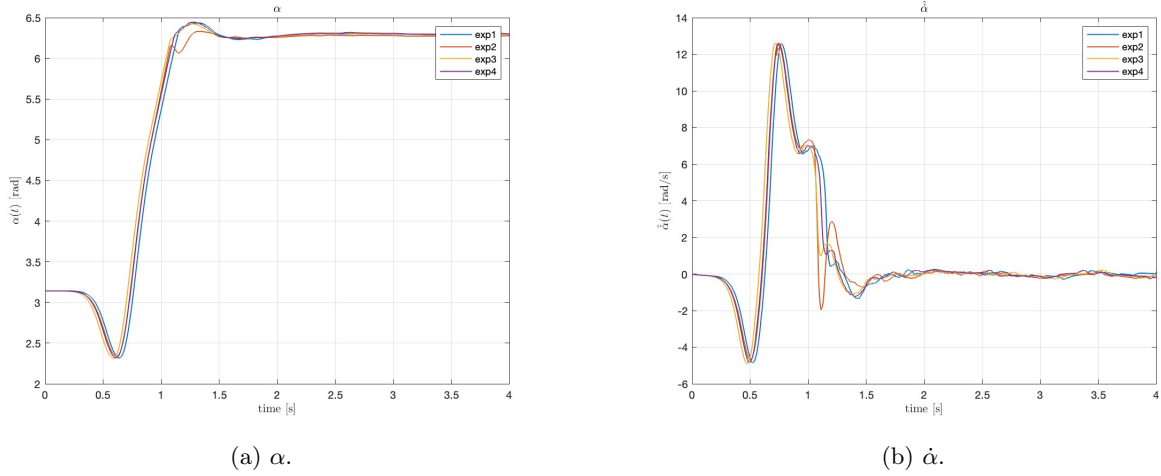


Figure 5.6:  $\alpha, \dot{\alpha}$  Experimental.

	$\alpha_{max}$ [rad]	$\alpha_{min}$ [rad]	$t_{switch}$ [s]	$\dot{\alpha}_{max}$ [rad/s]	$\dot{\alpha}_{min}$ [rad/s]
Exp.1	6.43	2.32	1.09	12.59	-4.86
Exp.2	6.33	2.34	1.05	12.59	-4.69
Exp.3	6.42	2.31	1.04	12.61	-4.90
Exp.4	6.44	2.32	1.06	12.60	-4.84

Table 5.6: Significant Values of  $\alpha$  and  $\dot{\alpha}$  during Swing Up.

## List of Figures

1	Rotatory Inverted Pendulum. . . . .	II
1.1	Free Body Diagram. . . . .	1
1.2	Simulated and Measured Angles $\theta$ and $\alpha$ . . . . .	5
2.1	Input Voltage for Training. . . . .	7
2.2	$\theta$ Angle in Training. . . . .	8
2.3	$\alpha$ Angle in Training. . . . .	8
2.4	$\theta$ Angle in Validation. . . . .	9
2.5	$\alpha$ Angle in Validation. . . . .	9
2.6	Chirp Input Voltage. . . . .	10
2.7	Chirp $\theta$ . . . . .	11
2.8	Chirp $\alpha$ . . . . .	11
2.9	Residual Analysis. . . . .	12
3.1	Bode Diagram of Eq. 3.3. . . . .	14
3.2	Bode Diagram of $L(s)$ . . . . .	15
3.3	Sensitivity Functions. . . . .	15
3.4	Frequency Based Control Scheme. . . . .	16
3.5	$G_{Y\alpha}(s)$ . . . . .	16
3.6	Step Response Performances. . . . .	17
3.7	Experimental Square Wave Response. . . . .	17
3.8	Resonance of $G_{Y\alpha}(s)$ . . . . .	18
4.1	General Control Scheme for a State Space Controller. . . . .	19
4.2	Pole Placement Controller in Simulation. . . . .	20
4.3	Luenberger Observer Simulation and Estimation. . . . .	21
4.4	LQ Controller in Simulation. . . . .	23
4.5	Kalman Filter Simulation and Estimation. . . . .	24
4.6	Different Reference for $\theta$ with Pole Placement Tracking Controller. . . . .	26
4.7	Different Reference for $\theta$ with LQG Tracking Controller. . . . .	27
4.8	Robustness of Tracking Controllers Under Impulsive Disturbances in Simulation. . . . .	28
4.9	Pole Placement Experiment for the Stabilization of $\alpha$ with Observer. . . . .	28
4.10	Pole Placement Experiment for the Tracking of $\theta$ with Observer. . . . .	29
4.11	Pole Placement Experiment for the Tracking of $\theta$ with Kalman Filter. . . . .	29
4.12	LQG Experiment for the Stabilization of $\alpha$ with Luenberger Observer. . . . .	30
4.13	LQG Experiment for the Stabilization of $\alpha$ with Kalman Filter. . . . .	30
4.14	LQG Experiment for the Tracking of $\theta$ with Luenberger Observer. . . . .	31
4.15	LQG Experiment for the Tracking of $\theta$ with Kalman Filter. . . . .	31
5.1	Input Voltage. . . . .	35
5.2	$\theta, \dot{\theta}$ Simulated and Experimental. . . . .	36
5.3	$\alpha, \dot{\alpha}$ Simulated and Experimental. . . . .	36
5.4	Input Voltage. . . . .	37
5.5	$\theta, \dot{\theta}$ Experimental. . . . .	37
5.6	$\alpha, \dot{\alpha}$ Experimental. . . . .	38

## List of Tables

2.1	Identified Parameters . . . . .	7
2.2	Comparison of fit % in Time Domain. . . . .	10
2.3	Comparison of M.S.E. in Frequency Domain. . . . .	11
2.4	$\alpha$ Resonance Peaks Magnitude and Frequency. . . . .	11
3.1	Open Loop Properties. . . . .	13
3.2	Regulator $R(s)$ Singularities. . . . .	14
3.3	Peaks and Bandwidths. . . . .	16
3.4	Specifications and Simulation of the Unitary Step. . . . .	17
3.5	Experimental and Simulated Results of the Closed Loop System. . . . .	18
4.1	Simulation Data. . . . .	20
4.2	Simulation Data. . . . .	23
4.3	Simulation Data. . . . .	26
4.4	Simulation Data. . . . .	27
4.5	Experimental Data. . . . .	32
5.1	Swing Up Saturation Specifications. . . . .	35
5.2	Significant Values of $\theta$ and $\dot{\theta}$ during Swing Up. . . . .	35
5.3	Significant Values of $\alpha$ and $\dot{\alpha}$ during Swing Up. . . . .	36
5.4	Swing Up Saturation Specifications. . . . .	37
5.5	Significant Values of $\theta$ and $\dot{\theta}$ during Swing Up. . . . .	37
5.6	Significant Values of $\alpha$ and $\dot{\alpha}$ during Swing Up. . . . .	38
5.7	Step Response Parameters. . . . .	42
5.8	System Parameters and Points. . . . .	43

## Bibliography

- [1] G. Garcia-Chavez and E. Muñoz-Panduro. Global control for the furuta pendulum based on partial feedback linearization and stabilization of the zero dynamics. In *2017 13th IEEE Conference on Automation Science and Engineering (CASE)*, pages 334–339, 2017.
- [2] X. Lai, J. She, S. Yang, and M. Wu. Stability analysis and control law design for acrobots. pages 745–750, 01 2006.
- [3] MathWorks. compare function, 2022.
- [4] MathWorks. Extended kalman filters, 2023.
- [5] Quanser. Rotary inverted pendulum, 2023.

# Appendix

## Formulas

$$\begin{bmatrix} 1 \times 10^{-4} \\ 2.2880 \\ 0.8100 \\ 0.6210 \\ 0.0068 \\ 0.0068 \end{bmatrix} \leq \begin{bmatrix} B_p \\ B_r \\ J_a \\ J_p \\ l_p \\ R_m \\ \eta_g \\ \eta_m \\ k_m \\ k_t \end{bmatrix} \leq \begin{bmatrix} 3 \times 10^{-3} \\ 3 \times 10^{-3} \\ 2.5 \times 10^{-3} \\ 1.7 \times 10^{-3} \\ 0.337 \\ 2.9120 \\ 0.9900 \\ 0.7590 \\ 0.0086 \\ 0.0086 \end{bmatrix} \quad (\text{A1})$$

$$\text{fit}(\%) = 100 \times \left(1 - \frac{\|\tilde{\mathbf{y}} - \hat{\mathbf{y}}\|}{\|\tilde{\mathbf{y}} - \text{mean}(\tilde{\mathbf{y}})\|}\right) \quad (\text{A2})$$

Parameter	Formula/Description
Rise Time ( $t_r$ )	Time required by the signal to pass from 10% to 90%
Settling Time ( $t_s$ )	Amount of time such that ( $e < 0.02  y_{final} - y_{initial} $ )
Overshoot (%)	$\frac{y_{max} - y_{final}}{y_{final}} 100$
Peak Time ( $t_p$ )	Time required by response to reach its first peak

Table 5.7: Step Response Parameters.

## Tables

	Symbol	Nominal Value	Units
Inertial frame origin	$O$		
C.o.m. $OB$ arm	$G_A$		
Pendulum rotational joint	$B$		
Mass $OB$ arm	$m_a$	0.257	kg
Inertia $OB$ w.r.t. $O$	$J_a$	$9.98 \times 10^{-4}$	$kg \times m^2$
Distance $OG_A$	$l_a$	0.0619	m
Distance $OB$	$r$	0.216	m
Pendulum c.o.m.	$G_P$		
Pendulum mass	$m_p$	0.127	kg
Pendulum Inertia w.r.t. $G_P$	$J_p$	0.012	$kg \times m^2$
$BG_P$ distance	$l_p$	0.156	m
Gravitational acc.	$g$	9.81	$m/s^2$
Motor torque	$\tau$		N
Arm joint viscous coefficient	$B_r$	0.0024	$Nms/rad$
Pendulum joint viscous coefficient	$B_p$	0.0024	$Nms/rad$
Gear-Box efficiency	$\eta_g$	0.90	
Motor efficiency	$\eta_m$	0.69	
Gear-Box ratio	$K_g$	70	
Motor Current-Torque constant	$k_t$	$7.68 \times 10^{-3}$	$Nm/A$
Input Voltage	$V_m$	6	V
Motor back e.m.f.	$k_m$	$7.68 \times 10^{-3}$	$V/(rad/s)$
Armature resistance	$R_m$	2.6	$\Omega$

Table 5.8: System Parameters and Points.